Published in final edited form as:

Nature. 2016 April 21; 532(7599): 323–328. doi:10.1038/nature17624.

Distinct bone marrow blood vessels differentially regulate hematopoiesis

Tomer Itkin[1], **Shiri Gur-Cohen**[1], **Joel A. Spencer**[2,3], **Amir Schajnovitz**[4,5,6], **Saravana K. Ramasamy**[7], **Anjali P. Kusumbe**[7], **Guy Ledergor**[1,8], **Yookyung Jung**[2,3], **Idan Milo**[1], **Michael G. Poulos**[9], **Alexander Kalinkovich**[1], **Aya Ludin**[1], **Orit Kollet**[1], **Guy Shakhar**[1], **Jason M. Butler**[9], **Shahin Rafii**[9], **Ralf H. Adams**[7], **David T. Scadden**[4,5,6], **Charles P. Lin**[2,3,#], and **Tsvee Lapidot**[1,#]

[1]Department of Immunology, The Weizmann Institute of Science, Rehovot, 76100, Israel;

[2]Wellman Center for Photomedicine, Massachusetts General Hospital, Harvard Medical School, Boston, MA 02114, USA;

[3]Center for Systems Biology, Massachusetts General Hospital, Harvard Medical School, Boston, MA 02114, USA;

[4]Department of Stem Cell and Regenerative Biology, Harvard University, Cambridge, MA 02138, USA;

[5]Harvard Stem Cell Institute, Cambridge, MA 02114, USA;

[6]Center for Regenerative Medicine and Cancer Center, Massachusetts General Hospital, Boston, MA 02114, USA;

[7]Max Planck Institute for Molecular Biomedicine, Department of Tissue Morphogenesis and Faculty of Medicine, University of Münster, D-48149 Münster, Germany;

[8]Internal Medicine Department, Tel-Aviv Sourasky Medical Center, Tel-Aviv, Israel;

[9]Department of Genetic Medicine, Weill Cornell Medical College, New York, NY, 10065, USA

Abstract

[#]**Correspondence should be addressed to**: Tsvee Lapidot, Department of Immunology, Weizmann Institute of Science, Rehovot, 76100, Israel. Tel: +972-8-934-2481 Tsvee.Lapidot@weizmann.ac.il, Charles P. Lin, Wellman Center for Photomedicine and Center for Systems Biology, Massachusetts General Hospital, Harvard Medical School, Boston, MA 02114, USA. Tel: +1-617-643-3531 charles_lin@hms.harvard.edu.

AUTHOR CONTRIBUTIONS:

T.I. designed and performed experiments, analyzed data and wrote the manuscript; S.G.C. helped in the design and execution of experiments and analyzed data; J.A.S., A.S., and J.Y. designed and performed intravital related experiment, analyzed data and helped writing the manuscript; S.K.R and A.P.K. designed and performed confocal related experiments and analyzed data; G.L., I.M., M.G.P., A.K., A.L., and O.K. helped with experiments; G.S. helped and guided in some intravital related experiments; J.M.B. and S.R. helped in design of endothelial related studies; R.H.A helped and guided in design of confocal and *in vivo* endothelial related experiments; D.T.S. helped and guided in design of *in vivo* intravital live imaging experiments and wrote the manuscript; and T.L. and C.P.L. guided and designed the research and wrote the manuscript.

Supplementary Information is linked to the online version of the paper at www.nature.com/nature.

The authors do not declare competing financial interests.

Bone marrow (BM) endothelial cells (BMECs) form a network of blood vessels (BVs) which regulate both leukocyte trafficking and hematopoietic stem and progenitor cell (HSPC) maintenance. However, it is not clear how BMECs balance these dual roles and if these events occur at the same vascular site. We found that BM stem cell maintenance and leukocyte trafficking are regulated by distinct BV types with different permeability properties. Less permeable arterial BVs maintain HSCs in a low reactive oxygen species (ROS) state, whereas the more permeable sinusoids promote HSPC activation and are the exclusive site for immature and mature leukocyte trafficking to and from the BM. A functional consequence of high BVs permeability is that exposure to blood plasma increases BM HSPC ROS levels, augmenting their migration capacity while compromising their long term repopulation and survival potential. These findings may have relevance for clinical hematopoietic stem cell transplantation and mobilization protocols.

Vascular forming endothelial cells form a vast network which participates in homeostasis and metabolism regulation, delivering oxygen, nutrients and other building blocks to distinct organs. This diverse network also serves as a cellular highway allowing trafficking of blood cells, leukocytes and other cell types throughout the body. In addition, endothelial cells serve an important role as regulators of organ homeostasis and regeneration via direct interactions with local stem and progenitor cells, and by secretion of angiocrine factors[1]. Bone marrow (BM) endothelial cells (BMECs) form a mechanical barrier, which prevents BM entry of mature red blood cells and platelets from the circulation, regulating cellular trafficking, hematopoiesis and osteogenesis[2–4]. BMECs also contribute to specialized perivascular microenvironments where the majority of BM hematopoietic stem and progenitor cells (HSPCs) reside[5–8]. BMEC perivascular domains include heterogeneous populations of mesenchymal stromal precursor cells (MSPCs) previously reported to regulate HSPCs[9–11]. In addition, BMECs provide angiocrine signals that regulate HSCs development and hematopoiesis[10,12,13]. Different types of blood vessels (BVs) compose the BM vascular network[4,11,12], exhibiting distinct properties and forming unique domains. We have set to investigate how do BMECs exert their dual roles as regulators of stem cell maintenance and of cellular trafficking, and if these distinct roles are associated with specialized BVs sub-types and specific micro-anatomical regions. We began by characterizing the BM vascular architecture, distinct BVs properties, and their associated “niche” cells participating in the formation of unique BM multi-cellular domains. Finally, we examined whether manipulation of endothelial properties may serve to control tissue homeostasis and stem cell fate.

Defining BM vascular architecture and domains

We used Ly6a(Sca-1)–EGFP transgenic mice to distinguish between Sca-1$^-$ sinusoidal BMECs (sBMECs) from Sca-1$^+$ arterial BMECs (aBMECs)[12]. Arterial BMECs (23.5±3.1% of BMECs, Fig. 1a) display unique elongated elliptical nuclear morphology (Fig. 1b). Adherence and tight junction molecules VE-cadherin and ZO-1 were highly and preferentially expressed by aBMECs (Fig. 1c and Extended Data Fig. 1a). Sca-1$^+$ BVs had smaller diameters compared to neighboring Sca-1$^-$ sinusoids and were closely associated with calcified bone at the metaphysis or in the diaphysis (Fig. 1d and Supplementary video 1). Arteries co-stained for Sca-1/CD31, were enwrapped by αSMA$^+$ pericytes (Fig. 1e). Approaching the endosteum arteries branched into smaller arterioles, which were not

associated with αSMA$^+$ pericytes but were instead surrounded by Sca-1$^+$ mesenchymal (reticular) and clusters of Sca-1$^+$ hematopoietic (round) cells (Fig. 1e). Combining osteopontin (OPN) staining for bone lining osteoblasts (Extended Data Fig. 1b), we show that the vast majority of arterial BVs are found at a distance of <40 μm from the endosteum, with ~50% at a closer distance of <20 μm from the endosteum (Extended Data Fig. 1c). Arteries enwrapped by αSMA$^+$ pericytes had ~10 μm diameter, branching to smaller ~5 μm diameter endosteal arterioles, connecting downstream to much larger ~25 μm sinusoids (Extended Data Fig. 1d).

High intracellular levels of reactive oxygen species (ROS) hamper BM HSC quiescence, accelerating their differentiation and exhaustion[14,15]. Elevated ROS levels also promote HSPC mobilization by activating their motility machinery[16,17]. Detecting intracellular ROS^{high} expressing cells (Extended Data Fig. 1e, f), we found lower frequencies of ROS^{high} cells adjacent to arteries (Fig. 1f I, II and Extended Data Fig. 1g), compared to sinusoids (Fig. 1f III and Extended Data Fig. 1f). SLAM HSPCs associated with sinusoids and positioned >20 μm from aBMECs (41/41), had either negative/low (26 of 41) or high (15 of 41) ROS levels (Extended Data Fig. 1h, i). In contrast, SLAM HSPCs associated with arteries were consistently negative for ROS staining (22 of 22) (Extended Data Fig. 1j). Of note, the ROS^{low} SLAM HSPCs distant from arteries, resided in close proximity to megakaryocytes (<20 μm) consistent with the quiescent megakaryocytic stem cell niche reports[18–20] (Extended Data Fig. 1h). In agreement with a recent study[21] we confirmed that, if their metabolic state is ignored, SLAM HSPCs had random localization among distinct BM regions (Extended Data Fig. 1k).

BMECs and neighboring MSPCs characterization

Since specific sub-types of endosteal BVs serve as regulatory niches for bone-forming MSPCs[4], we analyzed BVs for expression of pericyte and MSPC markers NG2 and nestin[9,11,13]. NG2 stained a heterogeneous population, negative and positive for Sca-1, enwrapping Sca-1$^+$ BVs (Extended Data Fig. 2a). Unexpectedly, Sca-1 staining on BM sections from nestin-GFP mice, reported to label HSC-supportive BM MSPCs[9], revealed the existence of nestin$^+$ BMECs with elongated nuclei expressing Sca-1 and VE-cadherin (Extended Data Fig. 2b, c). Nestin$^+$ precursor cells give rise to both endothelial and mesenchymal lineages[22], and we have occasionally detected very bright nestin$^+$/Sca-1$^-$ MSPCs[11] adjacent to nestin$^+$/Sca-1$^+$ BMECs (Extended Data Fig. 2b). Nestin$^+$/NG2$^+$ MSPCs were tightly associated with nestin$^+$/NG2$^-$ BVs (Extended Data Fig. 2d). Nestin$^+$ BVs are mostly small diameter, di-acetyl-low-density lipoprotein (LDL)-negative BVs, associated with calcified bone (Extended Data Fig. 2e and Supplementary video 2). Among CD45$^-$/CD31$^+$ BMECs, nestin expression was restricted to Sca-1$^+$/CD31^{high} aBMECs and was absent from Sca-1$^-$/CD31$^+$ sBMECs (Extended Data Fig. 2f, g). Nestin-GFP was also expressed by heterogeneous populations of mesenchymal[9] and hematopoietic[23] populations (Extended Data Fig. 2g). Nestin$^+$ BVs and MSPCs were predominantly detected at the metaphysis and adjacent to cortical bone at the diaphysis (Extended Data Fig. 2h, i). Of interest, nestin expressing non-myelinating Schwann cells that maintain hibernating HSC[24], were exclusively associated only arteries, contributing to metabolically “low” microenvironments (Extended Data Fig. 2j–l).

Further profiling expression of endothelial molecules involved in leukocyte trafficking, we noted that aBMEC express higher levels of VCAM-1, ICAM-1, P-selectin and preferentially expressed JAM-A, while sBMEC preferentially express higher levels of E-selectin (Extended Data Fig. 3a–f), which is involved in HSPCs BM homing[6]. In addition to their role in leukocyte trafficking, these adhesion molecules also control HSPC retention by VCAM-1[25] or negative regulation of HSC quiescence by E-selectin[26]. Endothelial metabolism, more specifically glycolysis rather than oxidative phosphorylation, regulates vessel development and function[27,28]. We noted that aBMEC exhibit lower ROS levels and higher glucose uptake relative to sBMEC (Extended Data Fig. 3g, h). This finding may indicate that aBMECs represent a more actively developing sub-type of BMEC and correlates with the observation that BM oxygen tension is highest near and in arterial BVs[29] skewing arteries to the glycolytic pathway to avoid excessive ROS production[28].

Sinusoids are the exclusive trafficking sites

Relatively to sinusoids, the preceding arterial nestin$^+$ BVs displayed lower permeability and dramatically higher blood flow and shear rates (Fig. 2a–f and Supplementary video 3–5). Comparing calvarial to femoral (including both diaphysis and metaphysis regions) bones, no major differences were noted in BV distribution, BV size, sinusoidal BV properties, or permeability, but the calvarial bone contained a higher frequency of BMECs, among them a higher frequency of aBMEC, displaying characteristics of enhanced integrity (Extended Data Fig. 4a–e).

Phenotypically defined long-term repopulating (LTR)-HSCs are reported to localize preferentially near nestin$^+$ stromal cells[9]. The lower permeability, the high- flow speed[29], and high shear rates in arterial nestin$^+$ BVs suggest that a different type of BV serves as a site for HSPCs and mature leukocyte trafficking and homing to the BM. We observed that hematopoietic cell rolling and adhesion events occurred exclusively in sinusoids (377 of 377 events, Supplementary video 6 and Extended Data Fig. 4f, g). Similarly, trans-endothelial migration of mature leukocytes and immature HSPCs occurred exclusively via sinusoids (observed in 309 of 309 events, Fig. 2g and Supplementary videos 7–10).

Endothelial CXCL12-CXCR4 in HSC mobilization

AMD3100 treatment, an agent that induces rapid HSPC mobilization[30] via shedding and release of chemoattractant cytokines, such as stem cell factor (SCF) and CXCL12, from BM cells into the blood[31,32], reduced vascular integrity and cytokine abundance, preferentially on sBMECs (Extended Data Fig. 5a–d). Furthermore, AMD3100 led to reduced CXCR4 phosphorylation by BMEC, 5 minutes post administration (Extended Data Fig. 5e). CXCR4 neutralization treatment increased vascular permeability as well (Extended Data Fig. 5f). However, since these antibodies also directly inhibit HSPC egress and mobilization[32], we specifically deleted CXCR4 in endothelial cells (eΔCXCR4, Extended Data Fig. 5g–j). Increased vascular permeability and enhanced HSPC egress were observed in eΔCXCR4 mice (Extended Data Fig. 5k–m). Supported by *in vitro* findings[33], our data indicate that CXCR4 signaling regulates BM vascular integrity and, as a consequence, HSPC trafficking.

Leaky endothelium promotes HSPC trafficking

To delineate a potential connection between BV permeability allowing penetration of blood plasma into the BM and HSC development, we compared BM residing SLAM LSK HSPCs with circulating SLAM LSK HSPCs in the peripheral blood (PB). ROS levels in PB circulating HSPCs were much higher relative to BM residing HSPCs (Fig. 3a). Short *in vitro* exposure of BM HSPCs to PB plasma augmented intracellular ROS levels resulting in their enhanced migratory capacity (Fig. 3b, c). Yet, it also enhanced the frequency of apoptotic HSPCs, slightly increased HSPC cycling, along with enhanced differentiation, leading to reduced LTR-HSC capacity (Fig. 3d, e and Extended Data Fig. 6a, b).

Next, we tested whether the state of endothelial integrity affects BM HSC fate. Fibroblast growth factor (FGF) signaling has important roles in long term repopulating HSCs (LTR-HSCs) maintenance and expansion[34,35] and in maintaining endothelial integrity[36,37]. Accordingly, we observed that induction of FGF signaling enhanced BM endothelial barrier integrity (Extended Data Fig. 6c–e). In addition it led to significant changes in BM vascular architecture (Extended Data Fig. 6f–j). As a consequence, HSPCs and MSPCs fates were affected, resulting with their expansion[34], reduced HSPCs and LTR-HSCs bi-directional trafficking, reduced MSPC differentiation and with a shift in HSPC metabolism (Extended Data Fig. 6k–q).

To segregate endothelial mediated effects, we specifically deleted FGFR1 and FGFR2 in endothelial cells (eΔFGFR1/2) (Extended Data Fig. 5g). Impairment in endothelial integrity (Extended Data Fig. 7a–c) was measured in eΔFGFR1/2 mice. In agreement with their impaired barrier status, eΔFGFR1/2 mice demonstrated increased HSPC bi-directional trafficking (Fig. 3f, g). In contrast to wild type (WT) mice, FGF-2 treatment of eΔFGFR1/2 mice failed to reduce or prevent this phenomenon (Fig. 3f, g). Also, this model of endothelial FGF loss of function displayed significant changes in BM vascular architecture and properties (Extended Data Fig. 7d–j).

Vascular integrity maintains BM stem cells

We next investigated BM HSC maintenance under conditions of impaired endothelial integrity. Endothelial barrier disruption in eΔFGFR1/2 mice led to a significant reduction in the numbers of HSPCs/LTR-HSCs and BM PαS MSPCs[38] (Fig. 4a–f). Both HSPCs and MSPCs displayed increased ROS levels (Fig. 4g, h) and the frequency of ROS^{high} cells surrounding BVs was increased (Fig. 4i and Extended Data Fig. 7k).

Along with elevation in ROS levels, glucose uptake was enhanced by both HSPCs and MSPCs (Extended Data Fig. 7m and 8a) in eΔFGFR1/2 mice, indicating an augmentation of the oxidative phosphorylation pathway in these populations. Similar to plasma exposed BM HSPCs, HSPCs derived from eΔFGFR1/2 mice BM exhibited a slight elevation in cycling state, a dramatic increase in apoptosis, and following transplantation, a differentiation skewing (Extended Data Fig. 7n–q). The functional role of elevated ROS levels in HSPCs from eΔFGFR1/2 mice was tested using the ROS scavenger N-acetyl-L-cysteine (NAC).

Prolonged NAC treatment restored normal levels of HSPC egress to the PB, and normal levels of BM HSPC and LTR-HSC in eΔFGFR1/2 mice (Extended Data Fig. 7r–t).

Since MSPC metabolism and glucose uptake regulate bone formation[39], and plasma-borne factors such as vitamin E can penetrate the BM and influence bone remodeling[40], we examined stromal development under conditions of a hampered endothelial BM barrier. Accelerated stromal differentiation at the expense of the MSPC pool was observed (Extended Data Fig. 8a–d) alongside with dramatic changes in the BM concentrations of the hormones calcitonin and parathyroid hormone (PTH), regulating bone formation and remodeling, responding to changes in endothelial integrity (Extended Data Fig. 8j–m).

We also applied a pharmacological model to disrupt endothelial integrity by infusing neutralizing anti-VE-cadherin antibodies (αVE-cad Ab, Extended Data Fig. 9a). This model mimicked our genetic model affecting HSPC bi-directional trafficking and LTR-HSC maintenance which were also ROS dependent (Extended Data Fig. 9b–k). Vascular architecture and stromal development were also severely altered in this model of barrier manipulation (Extended Data Fig. 7l, 8e–i, and 9l–q).

Discussion

In the current study we investigated the roles of BMECs as regulators of hematopoiesis. First, the existence of diverse vascular niches among them an endosteal-vascular niche is supported by data showing that less permeable endosteal BVs provide a microenvironment promoting ROS^{low} HSC maintenance (Summarized in Extended Data Fig. 10). In support, specialized aPC-secreting BM arteries retain $EPCR^{+}$ LTR-HSC via downregulation of nitric oxide production, enhancing adhesion and reducing migration[41]. These data sets add to previous reports that BrdU-retaining HSCs are mostly localized in endosteal regions[42], where HSCs are maintained in a quiescent mode[43,44]. We extend previous studies reporting similar niches at steady-state[21] and in irradiated transplanted recipient mice[8,45] being located mainly at trabecular regions between the endosteal surface and previously undefined BVs. Of interest an HSPC sub-population expressing α-catulin, which is also expressed by activated migrating endothelial cells[46], preferentially localize to BM peri-sinusoidal domains[47]. We found that many cell types participate and form the BM HSC niches, sharing overlapping cell surface markers, including different endothelial, mesenchymal, hematopoietic and neuronal cells. We identified distinct sinusoidal sites for leukocyte trafficking, where entry and exit from the circulation occurs and metabolic parameters such as ROS are regulated (Summarized in Extended Data Fig. 10). ROS augmentation at these sites is manifested by penetrating plasma, via fenestrated endothelium, probably carrying ROS inducing factors found in higher concentration in the blood affecting HSCs[17]. Our results suggest that prolonged HSC loitering in the PB might be hazardous for their stemness properties and should be taken into account for clinical mobilization protocols. This is similar to cases of extraphysiological driven oxygen shock which elevates ROS levels, reducing LTR-HSC capacity in favor of more committed, maturing progenitors[48]. Endothelial cells are exposed to the highest levels of physiological oxygen tension and therefore developed internal mechanisms to scavenge excessive ROS molecules and rely mainly on glycolysis to avoid ROS production via oxidative phosphorylation[28]. ROS levels

were not altered in BMECs in all our manipulation models (data not shown), and we confirmed direct NAC-mediated rescue of the HSC phenotype. Prolonged NAC treatment reduced HSPC egress to the PB however it had no effect on endothelial barrier integrity (Extended Data Fig. 9r–t). These results reveal how NAC pretreatment increases transplanted HSC BM engraftment[49,50], as it has no effect on barrier permeability, allowing proper HSPC BM homing, and it may also promote a ROS-low supportive stem cell retaining microenvironment. Lastly, we show that the dynamic and versatile endothelial barrier may offer strategies to control stem cell functions relevant for clinical stem cell mobilization and transplantation protocols to enhance HSPCs egress to the peripheral blood, to promote successful BM lodgment of transplanted HSCs, and to expand engrafting HSCs following transplantation, via restricting or permitting the degree of plasma penetration.

METHODS:

Animals:

C57BL/6 (CD45.2) mice were purchased from Harlan Laboratories (Rehovot, Israel). B6.SJL (CD45.1) mice were bred in-house. Transgenic Ly6a(Sca-1)-EGFP mice and transgenic ROSA26-EYFP reporter mice were purchased from Jackson Laboratories. Transgenic nestin-GFP mice were kindly provided by Grigori N. Enikolopov (Cold Spring Harbor Laboratory, USA). Transgenic c-Kit-EGFP mice were kindly provided by Sergio Ottolenghi (University of Milano-Bicocca, Italy). Transgenic VE-cadherin(Cdh5, PAC)-CreERT2 mice were kindly provided by Ralf H. Adams (Max Planck Institute for Molecular Biomedicine, Germany). Conditional mutants carrying loxP-flanked CXCR4 were kindly provided by David Scadden (Harvard University, Cambridge, USA). Conditional mutants carrying loxP-flanked FGFR1 and FGFR2 (FGFR1/2$^{lox/lox}$) mice were kindly provided by Sabine Werner (Institute of Cell Biology, Switzerland) and by David Ornitz (Washington University School of Medicine, USA). To induce endothelial specific Cre activity and gene inactivation/expression, adult VE-cadherin(Cdh5, PAC)-CreERT2 mice interbred with CXCR4$^{lox/lox}$ (eΔCXCR4) or FGFR1/2$^{lox/lox}$ (eΔFGFR1/2) or with ROSA26-EYFP mice (eYFP) were injected intraperitoneally (i.p.) with tamoxifen (Sigma, T5648) 1 mg/mouse/day for 5 days. Mice were allowed to recover for 4 weeks post tamoxifen injections prior to sacrifice and experimental analysis. Mice carrying only VE-cadherin(Cdh5, PAC)-CreERT2 transgene or the CXCR42$^{lox/lox}$/FGFR1/2$^{lox/lox}$ mutations were used as WT controls to exclude non-specific effects of Cre activation or of floxed alleles mutation. Endothelial FGFR1/2 deletion was confirmed by qRT-PCR measurements of CXCR4 and FGFR1/2 mRNA from isolated BMECs.

Male and female mice at 8–12 weeks of age were used for all experiments. All mouse offspring from all strains were routinely genotyped using standard PCR protocols. Sample size was limited by ethical considerations and background experience in stem cell transplantation (bone marrow transplantation) which exists in the lab for many years and other published manuscripts in the field of stem cells, confirming a significant difference between means. No randomization or blinding was used to allocate experimental groups and no animals were excluded from analysis. All mutated or transgenic mouse strains had a C57BL/6 background. All experiments were done with approval from the Weizmann

Institute Animal Care and Use Committee. Mice that were maintained at the Weizmann Institute of Science were bred under defined flora conditions. Two-photon *in vivo* microscopy procedures that were performed in Harvard Medical School were approved by the Institutional Animal Care and Use Committee at Massachusetts General Hospital.

In Vivo treatments

AMD3100 (Sigma-Aldrich) 5 mg/kg was administrated to mice by subcutaneous (s.c.) injection. Mice were sacrificed 30 min later.

Recombinant murine FGF-2 (ProSpec) 200 μg/kg was administrated to mice by i.p. injections for 7 consecutive days.

Neutralizing Rat anti VE-cadherin antibodies or Rat IgG (eBioscience) 50 μg/mouse/day were administrated to mice by intravenous (i.v.) injections for 2 or 5 days.

Neutralizing Mouse anti CXCR4 antibodies (12G5 clone) or Mouse IgG (eBioscience) 50 μg/mouse were administrated twice with 30min interval by intravenous (i.v.) injections.

To inhibit ROS production, the antioxidant N-acetyl-L-cysteine (NAC; Sigma-Aldrich) was administered by i.p. injection of 130 mg/kg for 2, 5 or 7 days. Mice were sacrificed 2–4 hours following last injection.

Immunofluorescence

For standard and confocal fluorescent microscopy femurs were fixed for 2 hours in 4% paraformaldehyde, replaced and washed with 30% sucrose, embedded in optimum cutting temperature compound and then ‘snap-frozen’ in *N*-methylbutane chilled in liquid nitrogen. Sections (5–10 μm) were generated with a CM1850 Cryostat (Leica) at −25°C with a tungsten carbide blade (Leica) and a CryoJane tape transfer system (Instrumedics), then were mounted on adhesive-coated slides (Leica), fixed in acetone and air-dried. Sections were stained by incubation overnight at 4°C with primary antibodies followed by 1 hour incubation of secondary antibody at room temperature (RT) and in some cases also nuclei labeling by Hoechst 33342 (Molecular Probes) for 5 minutes at RT. Standard analysis (5–6 μm sections) was performed with Olympus BX51 microscope and Olympus DP71 camera. Confocal analysis (10 μm sections) was performed using a Zeiss LSM-710 microscope. In some cases, for BMBVs morphological and phenotypical confocal analysis, femurs and tibias were fixed for 2 hours in 4% paraformaldehyde, decalcified with 0.5 M EDTA at 4°C with constant shaking, immersed into 20% sucrose and 2% polyvinylpyrrolidone (PVP) solution for 24 hours, then embedded and frozen in 8% gelatin (porcine) in presence of 20% sucrose and 2% PVP. Sections (80–300 μm) were generated using low-profile blades on a CM3050 cryostat (Leica). Bone sections were air-dried, permeabilized for 10 min minmimm in 0.3% Triton X-100, blocked in 5% donkey serum at RT for 30 min, and incubated overnight at 4 °C with primary antibodies. Confocal analysis was performed using a Zeiss LSM-780 microscope. *Z*-stacks of images were processed and 3D-reconstructed with Imaris software (version 7.00, Bitplane). As previously described[4], tile scan images were produced by combining the signal of multiple planes along the Z-stalk of bone sections to allow visualization of the distinct types of BM BVs and the cells in their surroundings. For the

quantifications of BV diameters, a region of 600–700 μm from the growth plate towards the caudal region was selected and diameters for arterial and sinusoidal BVs were calculated using the ImageJ software on the high-resolution confocal images.

Primary and secondary antibodies and their relevant information are indicated in the antibodies table.

For *in vivo* ROS detection in BM sections, mice were i.p. injected with hydroethidine (Life Technologies) 10 mg/kg, 30 min prior to their sacrifice. For *in vivo* LDL-uptake detection in BM sections, mice were i.v. injected with Dil-Ac-LDL (BTI) 20 μg/mouse, 4 hours prior to their sacrifice. Femurs were immediately collected and processed as mentioned earlier. BM section analysis for scoring ROS^{high} cells was performed using ImageJ software (Extended Data Fig. 1). Multiple sections (>16 per mouse) were generated and analyzed from at least 4 mice per group of experimental procedure, in order to confirm biological repeats of the observed data. In some cases images were processed to enhance the contrast in order to allow better evaluation of cellular borders and markers co-localization.

Imaris, Volocity (Perkin Elmer), Photoshop and Illustrator (Adobe) software were used for image processing in compliance with *Nature*'s guide for digital images.

Intravital confocal and multiphoton microscopy

For blood vessels imaging in the calvarium of Sca-1-EGFP and nestin-GFP mice, we used a microscope (Ultima Multiphoton; Prairie Technologies) incorporating a pulsed laser (Mai Tai Ti-sapphire; Newport Corp.). A water-immersed 20× (NA 0.95) or 40× (NA 0.8) objective (Olympus) was used. The excitation wavelength was set at 850–910 nm. For intravital imaging mice were anesthetized with 100 mg ketamine, 15 mg xylazine and 2.5 mg acepromazine per kg. During imaging, mice were supplied with oxygen and their core temperature was maintained at 37°C with a warmed plate. The hair on the skullcap was trimmed and further removed using urea-containing lotion and the scalp was incised at the midline. The skull was then exposed and a small steel plate with a cut-through hole was centered on the frontoparietal suture, glued to the skull using cyanoacrylate-based glue and bolted to the warmed plate. To visualize blood vessels, mice were injected i.v. with 2 μl of a 2 μM non-targeted nanoparticles solution (Qtracker® 655, Molecular Probes). In some cases, mice were i.v. injected with Dil-Ac-LDL (BTI) 40 μg/mouse, 2 hours prior to their imaging. We typically scanned a 50 μm-thick volume of tissue at 4 μm Z-steps. Movies and figures based on two-photon microscopy were produced using Volocity software (Perkin Elmer). For live imaging of blood vessels permeability and leukocyte BM trafficking we have applied previously described experimental procedures and a home built laser-scanning multiphoton imaging system[29], with some modifications. Anesthesia was slowly induced in mice via inhalation of a mixture of 1.5–2% isoflurane and O_2. Once induced, the mixture was reduced to 1.35% isoflurane. By making a U-shaped incision on the scalp, calvarial bone was exposed for imaging and placed with 2% methocellulose gel on it for refractive index matching.

For BM BVs permeability studies, mice were positioned in heated skull stabilization mount which allowed access to the eye for on-stage retro-orbital injection of 40–60 μl of 10 mg/ml

70 kDa Rhodamine-Dextran (Life Technologies). Nestin-GFP (excited at 840 nm) and confocal reflectance (at 840 nm) signals were used to determine a region of interest within the mouse calvarial bone marrow for measurement of permeability. Next, Rhodamine-Dextran was injected and was continuously recorded (30 frames/s) for the first 10 minutes after injection. After video acquisition mice were removed from the microscope and sacrificed by euthanasia with CO_2. In some cases following Dextran clearance, same mice were used for homing experiments to monitor leukocyte cell trafficking in regions and blood vessels that were defined as less or more permeable. For cell homing studies, mice were injected with 2×10^6 DiD-labeled (Life Technologies) Lineage depleted immature hematopoietic progenitor cells (Miltenyi depletion) and with 2×10^6 DiI-labeled (Life Technologies) BM MNC isolated from age matched C57BL/6 mice along with 150 μL of 2 nmol/100 μL Angiosense 750EX (Perkin Elmer) fluorescent blood pool imaging agent, immediately prior to mounting the mice on a heated stage of a separate confocal/multiphoton microscope. Intravital images of the mouse BM were collected for up to the first 3 hours after injection of the cells. After imaging, the mice were removed from the microscope and sacrificed by euthanasia with CO_2. Permeability, blood flow/shear rates and homing experiments were repeated n=3 mice each, measuring multiple BVs and events, each mouse regarded as independent experiment, in order to confirm biological repeats of the observed data. The contrast and brightness settings of the images in the figures were adjusted for display purposes only.

Permeability and cell homing quantification

For permeability studies, the RGB movies were separated into red (Rhodamine-Dextran), green (nestin-GFP), and blue (reflectance) grayscale image stacks. An image registration algorithm (Normalized Correlation Coefficient, Template Matching) was performed on the red stack using ImageJ (v. 1.47p) to minimize movement artifacts within the image stack. Manual selection of regions of interest (ROI) was performed immediately next to individual vessels within the focus. Permeability of the vessels was calculated using the following equation:

$$P = \frac{V}{A} \times \frac{dI}{dt} \times \frac{1}{I_{in} - I_{out}}$$

P is the permeability of the vessel, V is the volume of the ROI next to the vessel, A is the fractional surface area of the vessel corresponding to the ROI, dI/dt is the intensity of the dye in the ROI as a function of time, I_{in} is the intensity of the dye inside the corresponding vessel at the beginning of measurement, and I_{out} is the intensity of the dye in the ROI at the beginning of measurement. To calculate dI/dt for a given vessel, the change in intensity was measured within the ROI over time and linearly fit the first ~5–40 seconds of the data. The slope of this linear fit is dI/dt. The ROI intensity curve is only linear for the first 30–40 seconds after which it begins to plateau. For cell homing, the number of stationary cells from the calvarial bone marrow images was counted and categorized into two groups: adherent and extravasated. We categorized both cells within the lumen of the vessel and cells in the process of transmigration in the adherent category. Maximum intensity projections of multiple z-stacks of images were used to count the number of cells in the two categories.

When there was a gap between cells and vessels in the two-dimensional projection image, those cells were categorized as extravasated. If any part of a cell overlapped a vessel in the projection image, the corresponding three dimensional z-stack was viewed to determine if the cell had undergone extravasation. When it was unclear if a cell had extravasated, it was always categorized as adherent.

Blood flow speed and shear rate quantification

For the flow speed measurement RBCs were labeled with 15 μM CFSE for 12 minutes at 37°C in PBS supplemented with 1 g/L glucose and 0.1% BSA. About 0.6 billion RBCs were injected (i.v). 40 μl of RhodamineB-dextran 70 kDa (10 mg/ml) was retro-orbitally injected immediately before imaging for visualizing BM vasculature. Movies of confocal images of blood vessel (RhodamineB, excitation: 561 nm, emission: 573–613 nm) and labeled RBCs (CFDA-SE, excitation: 491 nm, emission: 509–547 nm) were taken with the speed of 120 frames/sec. Individual RBCs were traced over a couple of frames. Total displacement of the RBCs was measured by imageJ and the speed of blood flow was calculated by:

$$\frac{total\ displacement\ of\ RBC\ (\mu m)}{time\left(=number\ of\ frames\times\frac{1}{120}\ \mathrm{sec}\right)}$$

To calculate the shear rate we assumed that the vessels were straight (straight cylinder) and the blood is an ideal Newtonian fluid with constant viscosity. Under these conditions, the shear rate (du/dr) can be calculated by du/dr=8*u/d (u is the average blood flow speed which was measured by tracing labeled RBCs and d is the diameter of the blood vessel as measured using ImageJ).

Flow cytometry

Immunostaining signal intensity was analyzed with MacsQuant (Miltenyi, Germany) or with a FACS LSRII (BD Biosciences) with FACSDiva software, data were analyzed with FlowJo (Tree Star). Data of molecules expression by cells was analyzed and presented as MFI (mean fluorescent intensity). To acquire single BM cell suspension, freshly isolated bones were cleaned, flushed and crushed using liver digestion medium (LDM, Invitrogen) supplemented with 0.1% DNaseI (Roche) and further digested for 30 minutes at 37°C, under shaking condition. Following incubation time, cells were filtered and washed extensively. To isolate and acquire mononuclear cells (MNC) from the peripheral blood PB, blood was collected from the heart using heparinized syringes and ficolled. Isolated BM and PB MNC cells underwent red blood cell lysis (Sigma) before staining. Cells were stained for 30 minutes at 4°C in standard flow cytometry buffer with primary and where indicated with secondary antibodies. Primary and secondary antibodies and their relevant information are indicated in the antibodies table.

For antigens that required intracellular staining, cell surface staining was followed by cell fixation and permeabilization with the Cytofix/Cytoperm kit according to the manufacturer's instructions (BD Biosciences). In case of internal GFP labeled cells, cells were fixed for 20 min with 4% PFA at RT, washed and incubated at RT for 1 hour in 30% sucrose. Cells were washed with flow cytometry buffer and further permeabilized. For intracellular ROS

detection cells were incubated for 10 minutes at 37°C with 2 μM hydroethidine (Life Technologies). For glucose uptake detection cells were incubated for 30 minutes at 37°C with the glucose analog 2-NBDG (Life Technologies). For detection of apoptotic cells, cells were resuspended in AnnexinV binding buffer (Biolegend) and stained with Pacific Blue AnnexinV (Biolegend).

ImageStream analysis

BM cells were enriched for lineage negative population, prepared as indicated for flow cytometry and analyzed using an ImageStreamX (Amnis) machine. Samples were visualized and analyzed for the expression of markers and antigens with IDEAS 4.0 software (Amnis). Single-stained control cells were used to compensate fluorescence between channel images. Cells were gated for single cells with the area and aspect ratio features or, for focused cells, with the Gradient RMS feature. Cells were then gated for the selection of positively stained cells only with their pixel intensity, as set by the cutoff with IgG and secondary antibody control staining. At least 5 samples from 5 mice were analyzed to confirm biological repeats of observed data.

Calcitonin and PTH ELISA kit assays

Detection of mouse calcitonin (Cusabio) and mouse PTH (Cloud-Clone Corp.) levels in BM supernatants was performed accordingly to manufacturer's instructions.

CFU assays

CFU-GM and CFU-F assays were previously described[34]. For CFU-Ob assay (also known as mineralized nodule formation assay), CFU-F medium was supplemented with 50 μg/ml ascorbic acid and with 10 mM β-glycerophosphate. After 3 weeks cultures were washed, fixed and stained using Alizarin red for mineralized matrix. The area of mineralized nodules per cultured well was quantified based on image analysis using ImageJ.

In vitro assays

BM cells were isolated after sterile bones flushing, crushing and digestion (as previously described). After washing, total BM cells were incubated in medium supplemented with or without 25% blood plasma or supplemented with 20 ng/ml TGFβ1 (ProSpec) for 2 hours. Plasma was isolated and collected from the upper fraction acquired from the peripheral blood after 5 min centrifugation at 1500 rpm.

In vivo Evans blue dye BM penetration assay

BM vascular endothelial barrier function was assessed using the Evans Blue Dye (EBD) assay. Evans Blue (Sigma-Aldrich) 20 mg/kg was injected i.v. 4 hours before mice were sacrificed. In each experiment a non-injected mouse was used for blank measurements. Subsequently, mice were perfused with PBS via the left ventricle to remove intravascular dye. Femurs were removed and formamide was used for bone flushing, crushing and chopping. EBD was extracted in formamide by incubation and shaking of flushed and crushed fractions, for overnight at 60° C. After 30 min centrifugation at 2000G, EBD in BM supernatants was quantitated by dual-wavelength spectrophotometric analysis at 620 nm and

740 nm. This method corrects the specimen's absorbance at 620 nm for the absorbance of contaminating heme pigments, using the following formula: corrected absorbance at 620 nm = actual absorbance at 620 nm – (1.426(absorbance at 740) + 0.03). Samples were normalized by subtracting blank measurements. BM penetration of EBD was expressed as OD620/Femur and the fold change in EBD BM penetration was calculated by dividing one of controls OD620/Femur from the rest of the samples per experiments. Finally, values were normalized per total protein extract from as determined by Bradford per sample.

Transplantation assays

For competitive LTR assay, B6.SJL (CD45.1) recipient mice were lethally irradiated (1000 cGy from a cesium source) and injected 5 hours later with $2X10^5$ donor derived (C57BL/6 background, CD45.2) BM cells or with 500μL volume of donor derived whole blood together with $4X10^5$ recipient derived (CD45.1) BM cells. Recipient mice were sacrificed 24 weeks post transplantation to determine chimerism levels using flow cytometry analysis. For calculation of competitive repopulating units (CRU), recipient mice were transplanted with limiting dilutions of donor derived BM cells ($2.5X10^4$-$2X10^5$) together with $2X10^5$ recipient derived BM cells. Mice were sacrificed after 24 weeks and multi-lineage myelo-lymphoid donor derived contribution in the PB was assessed using flow cytometry analysis. HSC-CRU frequency and statistical significance was determined using ELDA software (http://bioinf.wehi.edu.au/software/elda/).

In vivo homing assay

Lineage negative cells were enriched from total BM cells, taken from c-Kit-EGFP mice, using mouse lineage depletion kit (BD) according to the manufacturer's instructions. Non-irradiated recipient mice were transplanted by i.v. injection with $2.5X10^6$ c-Kit-EGFP labeled Lin^- cells. Recipient mice were sacrificed 4 hours post transplantation. BM cells were isolated from femurs and stained for flow cytometry as described above. Femur cellularity was determined in order to calculate the number of homed $CD34^-$/LSK HSPC per femur.

Quantitative real time RT-PCR to BMECs

For magnetic isolation of BMECs, freshly recovered bones were processed under sterile conditions as described for BMECs flow cytometry analysis, and post-digestion incubated with biotin rat anti-mouse CD31 antibodies (BD pharmigen) for 30 min at 4°c. Next, cells were washed and incubated with streptavidin particles plus (BD Imag) for 30 min at 4°c. Positive selection was performed using BD IMagnet (BD) according to the manufacturer's instructions (BD Biosciences). BD IMag buffer (BD) was used for washing and for antibodies dilution. Isolated cells were seeded on fibronectin (sigma-Aldrich) coated wells and cultured overnight in EBM-2 medium (Lonza) supplemented with EGM-2 SingleQuots (Lonza) at 37°c 5% CO_2. Non-adhesive cells were removed and adherent cells were collected using accutase (eBioscience). Flow cytometry was applied to confirm endothelial identity and >90% purity of recovered cells. BMEC were further processed to isolate RNA. Total RNA was isolated using TRI-Reagent (Sigma-Aldrich) according to the manufacturer's protocol. An aliquot of 2 μg of total RNA was reverse-transcribed using Moloney murine leukemia virus reverse transcriptase (Promega, Madison, WI) and oligo-dT

primers (Promega). Quantitative reverse transcribed–polymerase chain reaction (qRT-PCR) was done using the ABI 7000 machine (Applied Biosystems, Foster City, CA) with SYBR Green PCR Master Mix (Applied Biosystems). Comparative quantization of transcripts was assessed relative to hypoxanthine phosphoribosyl transferase (HPRT) levels and amplified with appropriate primers. Primer sequences used were as follows (mouse genes):

CXCR4 Forward 5'- ACGGCTGTAGAGCGAGTGTT-3'

Reverse 5'- AGGGTTCCTTGTTGGAGTCA-3'

FGFR1 Forward 5′-CAACCGTGTGACCAAAGTGG-3′

Reverse 5′-TCCGACAGGTCCTTCTCCG-3′

FGFR2 Forward 5′-ATCCCCCTGCGGAGACA-3′

Reverse 5′-GAGGACAGACGCGTTGTTATCC-3′

HPRT Forward 5′-GCAGTACAGCCCCAAAATGG-3′;

Reverse 5′-GGTCCTTTTCACCAGCAAGCT-3′.

Statistical analysis

All statistical analyses were conducted with Prism 4.0c version or Excel (*P < 0.05, **P < 0.01, ***P < 0.005, "n.s." represents non significance). All data are expressed as mean ± standard error (s.e.m) and all n numbers represent biological repeats. Unless indicated otherwise in figure legends, a Student's two-tailed unpaired t-test was used to determine the significance of the difference between means of two groups. One-way ANOVA or two-way ANOVA was used to compare means among three or more independent groups. Bonferroni post-hoc tests were used to compare all pairs of treatment groups when the overall P value was <0.05. A normal distribution of the data was tested using the Kolmogorov–Smirnov test if the sample size allowed. If normal-distribution or equal-variance assumptions were not valid, statistical significance was evaluated using the Mann-Whitney test and the Wilcoxon signed rank test. Animals were randomly assigned to treatment groups. Tested samples were assayed in a blinded fashion.

Extended Data

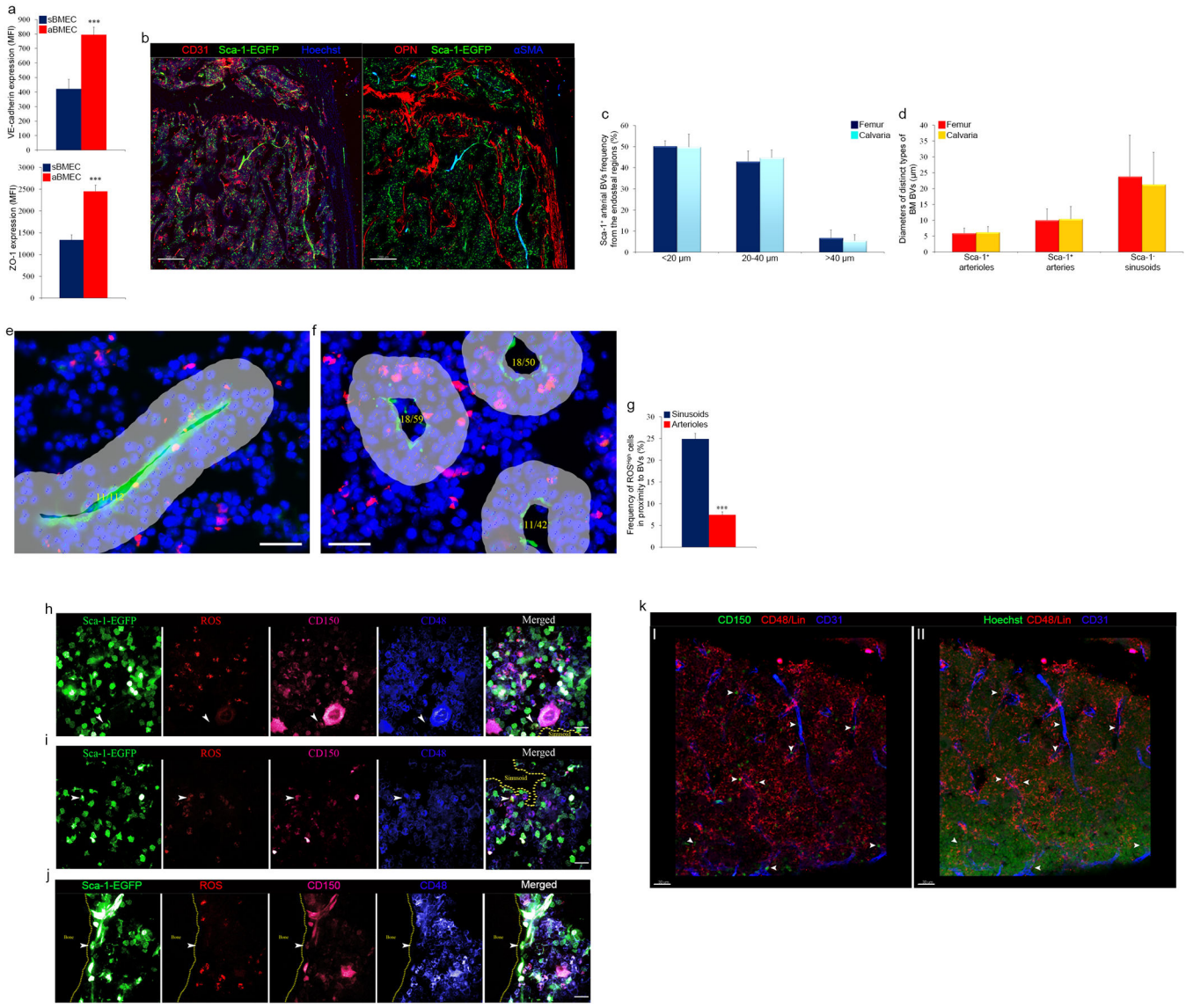

Extended Data figure 1:

a, Flow cytometry quantitative analysis of VE-cadherin and ZO-1 MFIs by BMEC sub-populations. (Mean ± s.e.m., n=9 mice from three independent experiments). P-values, two-tailed student's t-test (***P<0.005). **b**, Representative confocal image showing CD31(red)/ Sca-1^{+} (green) arterial BVs on proximity to endosteal regions in the metaphysis and representative confocal image of endosteal regions in the metaphysis showing Sca-1^{+} (green) arterial BVs, αSMA^{+} (blue) pericytes, and OPN (red) for endosteal borders. Scales indicate 200 μm. **c**, Frequencies of Sca-1^{+} arterial BVs distribution among zones representing growing distances from the endosteum in the calvaria and femur. **d**, Average diameters of distinct types of BVs in the clavarial and femoral marrow. **e-f**, Representative images of arterial BV (green, left) and of sinusoidal BVs (green, right) explaining how frequency of ROS^{High} cells around these BVs was scored. The gray-masked areas

surrounding the BVs indicate the region of distance <20 μm from the BVs. Odd numbers (1, 3, and 5) tag the nuclei of cells (blue) found in the region of interest while even numbers (2, 4, and 6) tag ROS^{High} (red) cells in the region of interest. ImageJ cell counter plugin was used to analyze and score the number of total cells and ROS^{High} cells in the region of interest. Yellow numbers in the center of the BVs indicate how many ROS^{High} cells are scored out of total cells. Scale bar indicates 20 μm. **g**, Frequency of ROS^{high} cells scored among total BM cells found in proximity (<20 μm) to different BM BVs. (Mean ± s.e.m., n=24 BM sections were analyzed from n=6 mice). P-values, two-tailed student's t-test (***P<0.005). **h-k**, White arrow heads indicate for SLAM HSPC **h**, Representative confocal images with ROS probe (red) of ROS$^{low/-}$, CD150^{+} (pink)/CD48^{-} (blue) SLAM HSPC, found away (>20 μm) from Sca-1^{+} (green) endosteal BVs, neighboring a megakaryocyte. Yellow dashed line indicates sinusoidal borders. Scale bar indicates 20 μm. **i**, Representative confocal images of ROS^{high} (red), CD150^{+} (pink)/CD48^{-} (blue) SLAM-HSPC, found away (>20 μm) from Sca-1^{+} (green) endosteal BVs, surrounded by mature hematopoietic cells. Yellow dashed line indicates for sinusoidal borders. Scale bar indicates 20 μm. **j**, Representative confocal images of cells with ROS^{High} (red) levels among CD150^{+} (pink)/CD48^{-} (blue) SLAM-HSPC neighboring (<20 μm) Sca-1^{+} (green) endosteal arteriole. Scale bar indicates 20 μm. **k**, Representative tile scan confocal images of BM merged Z-stalk showing **(I)** CD31^{+} BVs (blue) and their neighboring CD150^{+} (green) CD48/Lin (red) negative SLAM HSPC. **(II)** Cells nuclei are visualized (green) together with CD48/Lin (red) and CD31^{+} BVs (blue). Scale bars indicate 30 μm.

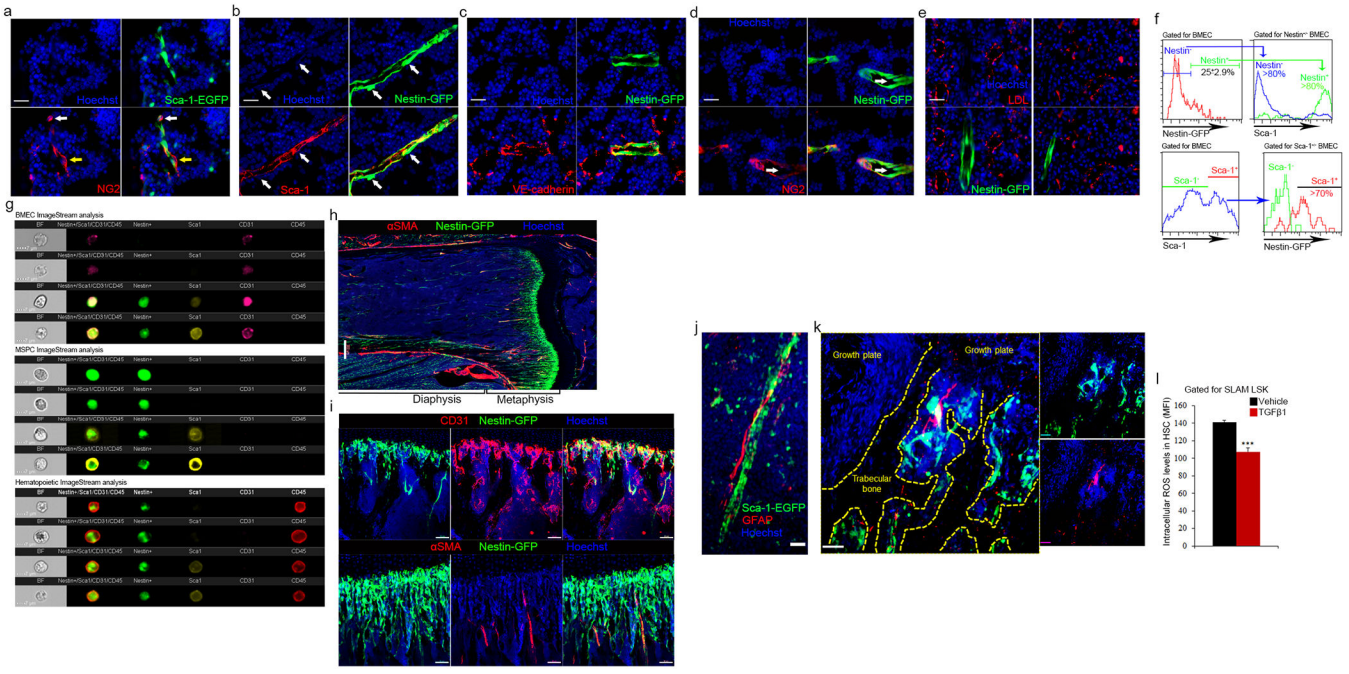

Extended Data figure 2:

a, Representative fluorescence images of Sca-1^{+} (green) BVs and their neighboring NG2^{+} (red) MSPCs. NG2^{+} MSPCs were either negative (yellow arrow) or positive (white arrow) for Sca-1 expression. Scale bar indicates 20 μm. **b**, Representative fluorescence images of

Sca-1$^+$ (red) BVs and nestin-GFP labeling (green) BVs and MSPCs (white arrows). Scale bar indicates 20 μm. **c**, Representative fluorescence images of nestin$^+$ (green) BVs and VE-cadherin (red) staining, showing that nestin$^+$ BV structures are co-stained with VE-cadherin while neighboring sinusoids are VE-cadherin$^+$/nestin$^-$. Scale bar indicates 20 μm. **d**, Representative fluorescence images of nestin$^+$ (green) BVs and their neighboring NG2$^+$ (red) MSPCs. NG2$^+$/nestin$^+$ MSPCs surrounded NG2$^-$/nestin$^+$ aBMECs with elongated nuclei (white arrow). Scale bar indicates 20 μm. **e**, Representative fluorescence images of large- and small-diameter nestin$^+$ (green) BVs and BVs positive for LDL (red) uptake, indicating that nestin$^+$ labels arteries and arterioles but not sinusoids. Scale bar indicates 20 μm. **f**, Representative flow cytometry histogram plots for gated BMECs, showing nestin-GFP expression on BMEC subpopulation which is Sca-1$^+$ or nestin-GFP expression by Sca-1$^{+/-}$ BMEC subpopulation. (Mean ± s.e.m., n=6 mice from three independent experiments). **g**, Representative ImageStream images of CD45$^-$/CD31$^+$/Sca-1$^-$/nestin$^-$ sBMECs and CD45$^-$/CD31$^+$/Sca-1$^+$/nestin$^+$ aBMECs, CD45$^-$/CD31$^-$/Sca-1$^{+/-}$/nestin$^+$ MSPCs, and CD45$^+$/CD31$^-$/Sca-1$^{+/-}$/nestin$^+$ hematopoietic cells. **h**, Representative confocal tile scan of nestin-GFP (Green) femur stained with αSMA (red). Scale bar indicates 200 μm. **i**, Representative confocal images of endosteal regions in the metaphysis showing αSMA (red) enwrapped nestin$^+$ (green)/CD31$^+$ (white) arterial blood vessels branching into smaller endosteal nestin$^+$/CD31$^+$ arterioles which are not associated with αSMA$^+$ pericytes. Endosteal nestin$^+$ BVs are surrounded by nestin$^+$ MSPCs. Scale bars indicate 50 μm. **j-k**, Representative confocal images of diaphysial area (a) and metaphysial area (b) showing GFAP (red, Schwann cell marker) fibers associated with Sca-1$^+$ (green) arterial BV (a) or with Sca-1$^+$ endosteal arterioles (b). Scale bar indicates 50 μm for (a) and 100 μm for (b). **l**, BM cells were incubated with 20 ng/ml TGFβ1 or vehicle for 2 h. ROS MFI levels in BM SLAM HSPCs were determined by flow cytometry quantitative analysis. (Mean ± s.e.m., n=9 repeats in triplicates from three independent experiments). P-values, two-tailed student's t-test (***P<0.005).

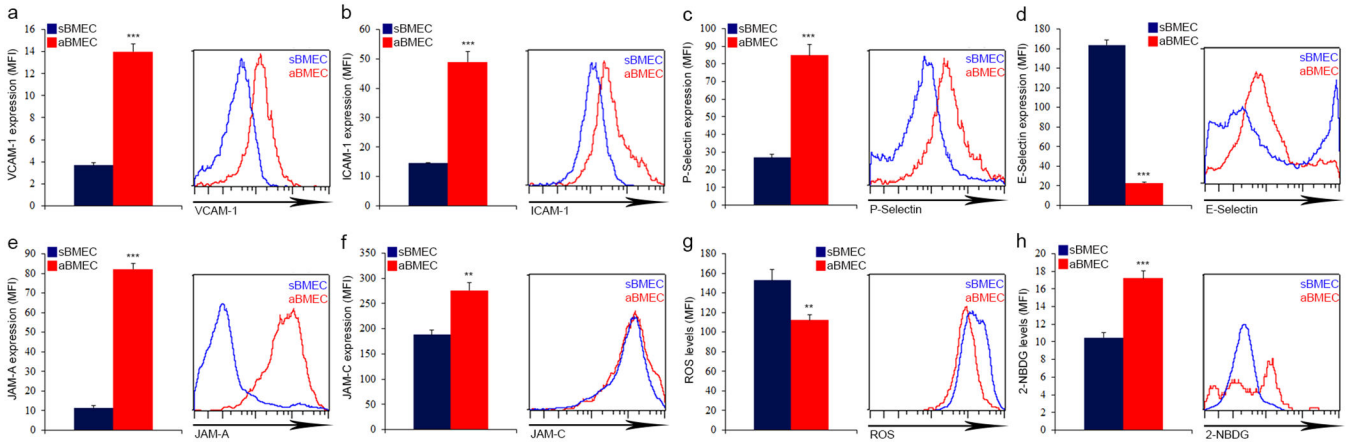

Extended Data figure 3:

a-h, Expression levels (MFI) of indicated surface or intracellular molecules by distinct types of BMEC as measured by flow cytometry analysis. (Mean ± s.e.m., n=8 Sca-1-EGFP mice

from two independent experiments). P-values, two-tailed student's t-test (**P<0.01, ***P<0.005).

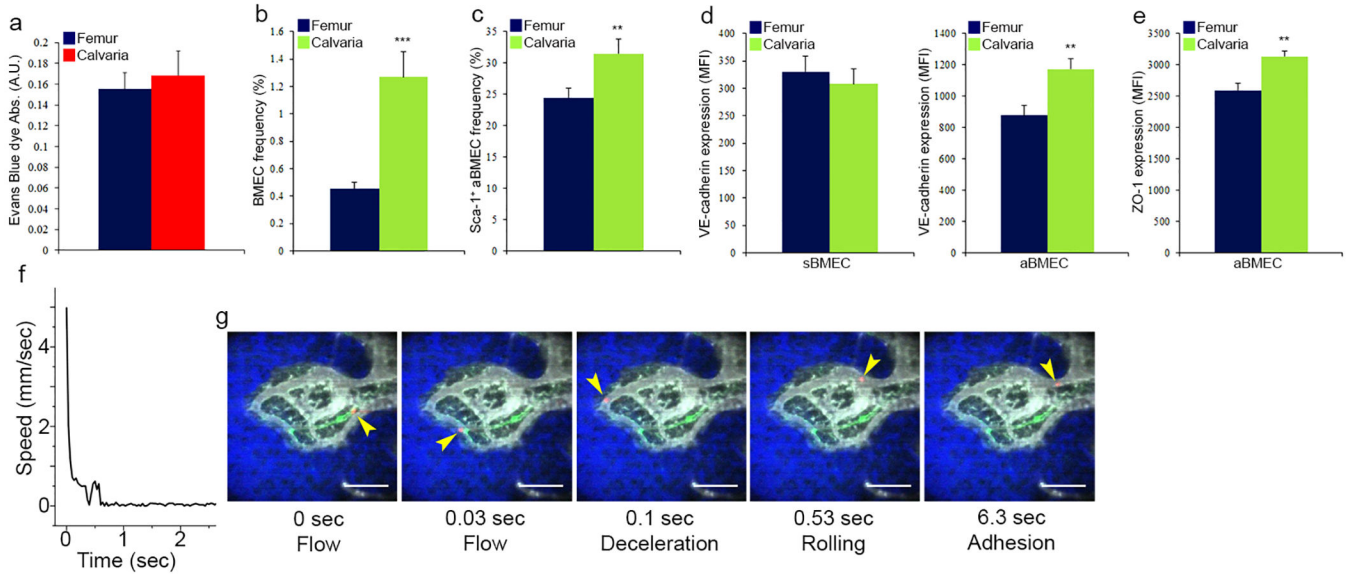

Extended Data figure 4:

a, Evans blue dye (EBD) absorbance following extraction from the femurs or calvarias, was measured using spectrophotometric analysis at 620 nm and 740 nm and normalized to total protein content per femur (Bradford). (Mean ± s.e.m., n=6 mice from two independent experiments).**b-e**, (Mean ± s.e.m., n=8 mice from two independent experiments). P-values, two-tailed student's t-test (**P<0.01, ***P<0.005). **b**, Total BMEC frequency as determined by flow cytometry analysis. **c**, Sca-1^{+} aBMEC frequency as determined by flow cytometry analysis. **d-e**, VE-cadherin and ZO-1 expression (MFI) on distinct types of BMECs as determined by flow cytometry analysis. **f**, A representative plot showing the flow speed of an HSPC passing through a network of nestin-GFP$^{+/-}$ BVs as a function of time. Note that the cell temporarily stops within a sinus at ~0.4 s and slowly roles until it adheres again at ~0.7 s. **g**, Snapshot images from 0, 0.03, 0.10, 0.53, and 6.3 s taken from Supplementary video 5. Nestin-GFP (green), HSPC (red), blood vessels (gray), and bone (blue) are displayed. The cell is overlaid on the pre-acquired nestin-GFP, blood vessels, and bone images. Yellow arrows indicate for the location of the trafficking HSPC. Scale bars indicate 100 μm.

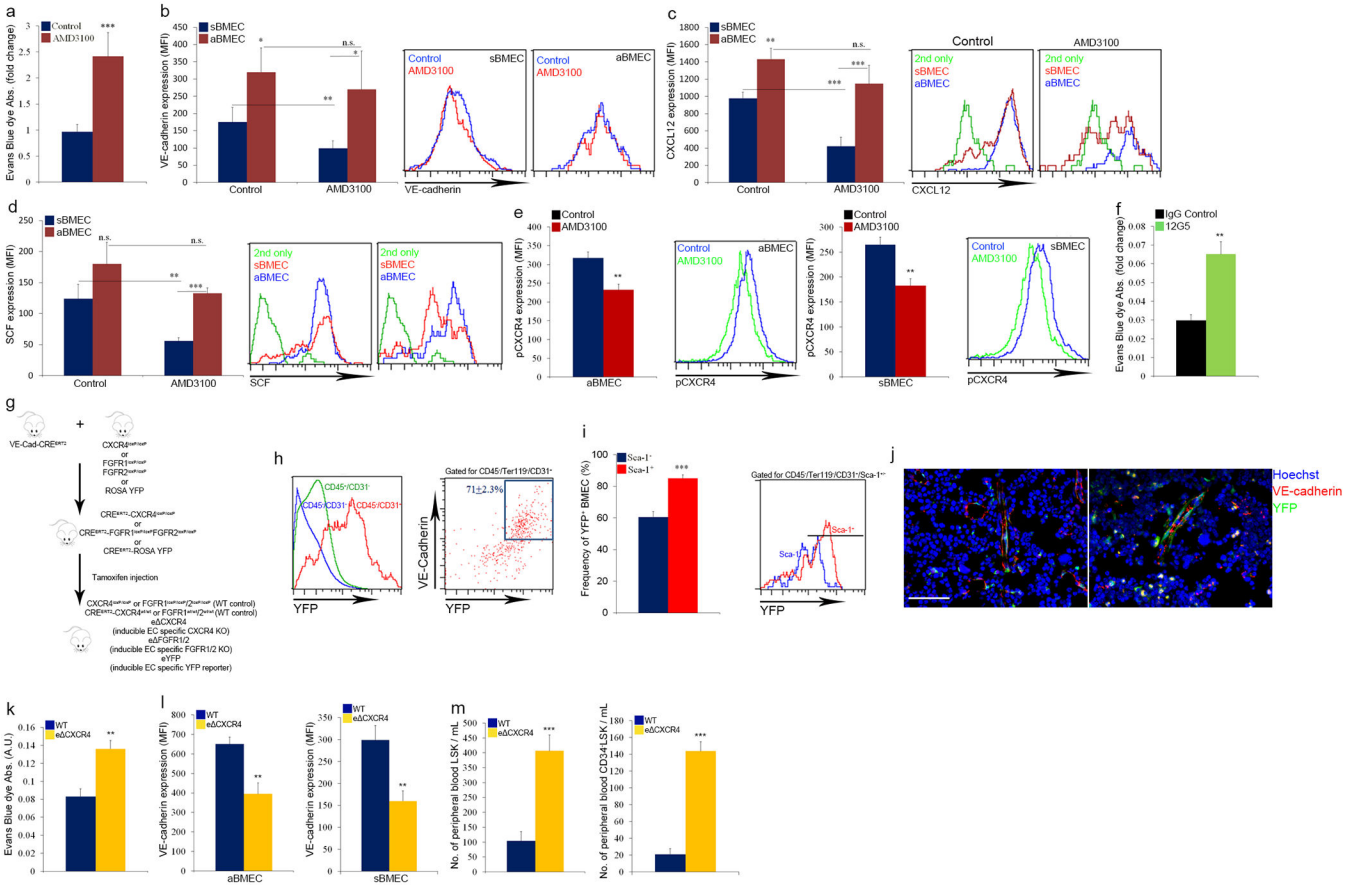

Extended Data figure 5:

a-e, C57BL/6 or nestin-GFP mice received a single injection of AMD3100 (5 mg/kg) and were analyzed 5 min (for pCXCR4) or 30 min later. (Mean ± s.e.m., n=7 mice from three independent experiments). P-values, two-way ANOVA with Bonferroni's multiple comparison post-hoc test (*P<0.05, **P<0.01, ***P<0.005). **a**, Evans blue dye (EBD) absorbance following EBD (30 mg/kg) injection together with AMD3100. **b-d**, Flow cytometry quantitative analysis and representative histogram plots of VE-cadherin, membrane-bound CXCL12, and membranal SCF MFIs. **e**, Intracellular CXCR4 phosphorylation (pCXCR4) levels (MFI) in distinct types of BMECs as measured by flow cytometry analysis and representative histogram plots. **f**, C57BL/6 mice received two injections (30 min interval) of 50 μg 12G5 CXCR4 neutralizing antibodies or IgG control followed by EBD injection. EBD absorbance following extraction from the femur was measured using spectrophotometric analysis at 620 nm and 740 nm. (Mean ± s.e.m., n=6 mice from two independent experiments). P-values, two-tailed student's t-test (**P<0.01). **g**, Endothelial cell (EC)-specific inducible deletion of CXCR4 (eΔCXCR4) or FGFR1/2 (eΔFGFR1/2) in mice. Mice harboring loxP sites flanking CXCR4 or FGFR1 and FGFR2 genes were crossed with a mouse line with endothelial-cell-specific VE-cadherin promoter-driven CreERT2 (VE-cadherin(Cdh5, PAC)-CreERT2). Specificity of VE-cadherin(Cdh5, PAC)-CreERT2 was validated in reporter mice carrying enhanced YFP protein following floxed stop codon (eYFP). CXCR4 or FGFR1/2 deletion or YFP expression in endothelial

cells was induced by tamoxifen injection. Mice analysis was performed 4 weeks post tamoxifen-induced Cre activity. Mice carrying only the CXCR4$^{lox/lox}$ or FGFR1/2$^{lox/lox}$ mutations or VE-cadherin(Cdh5, PAC)-CreERT2 transgene served as controls. **h-j**, (Mean ± s.e.m., n=12 mice from four independent experiments). P-values, two-tailed student's t-test (***P<0.005). **h**, Representative flow cytometry histogram and dot plots confirming BMEC specific induction of Cre activity by exclusive expression of YFP in ~70% of BMEC. **i**, Frequency of YFP expression and representative histogram plot, among BMEC sub-populations, was determined by flow cytometry quantitative analysis 4 weeks post tamoxifen induction of Cre activity. Note higher Cre activity, indicated by higher YFP signal, in aBMECs. Black line indicates for a positive signal region. **j**, Fluorescent representative images of YFP expression by distinct BMBVs (sinusoids and arteries). **k-m**, Tamoxifen treated WT and eΔCXCR4 mice were allowed to recover for 4 weeks before studies. (Mean ± s.e.m., n=9 mice from three independent experiments). P-values, two-tailed student's t-test (*P<0.05, ***P<0.005, **P<0.01). **k**, EBD absorbance in WT and eΔCXCR4 mice. **l**, Flow cytometry quantitative analysis of VE-cadherin MFI on BMEC from WT and eΔCXCR4 mice. **m**, Flow cytometry quantitative analysis of blood LSK HSPCs and CD34^{-}LSK HSPCs of WT or eΔCXCR4 mice.

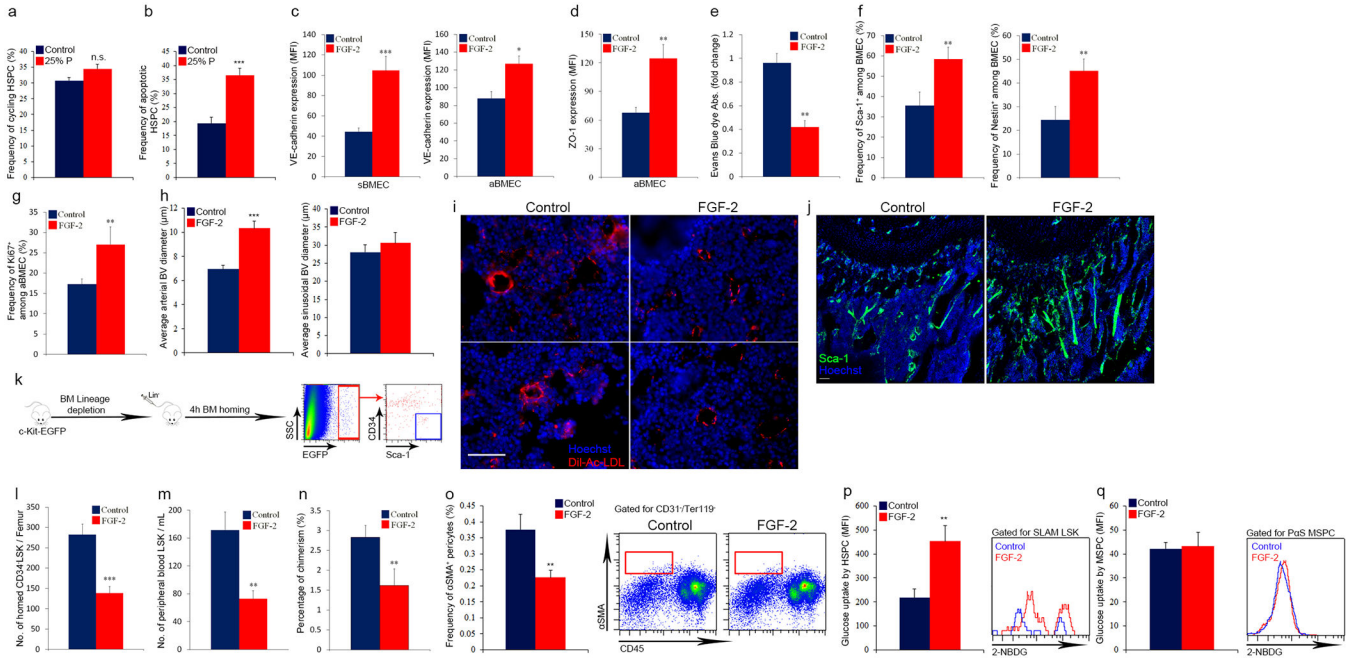

Extended Data figure 6:

a-b, BM cells were incubated for 2h with (25% P) or without (control) PB plasma. (Mean ± s.e.m., n=9 repeats from three independent experiments). P-values, two-tailed student's t-test (***P<0.005). **a**, Frequencies of cycling Ki67^{+} SLAM LSK HSPC. **b**, Frequencies of apoptotic AnnexinV^{+} SLAM LSK HSPC. **a-f**, C57BL/6 or nestin-GFP mice were treated with FGF-2 (200 μg/kg) for 7 days. (Mean ± s.e.m., n=9 mice from three independent experiments). P-values, two-tailed student's t-test (*P<0.05, ***P<0.005, **P<0.01). **c-d**, Quantitative analysis of VE-cadherin and ZO-1 MFIs on BMECs. **e**, EBD absorbance. **f-g**, Flow cytometry quantitative analysis of BMEC frequencies expressing Sca-1, nestin and

intracellular Ki67 cell cycling marker. **h**, Diameters of distinct types of BM BVs in the metaphysis region as determined by ImageJ software analysis of high-resolution confocal images. **i**, Fluorescent representative images of LDL (red) up-taken by sinusoidal BMEC and other BM cells following diffusion into the parenchymal marrow. Note lower LDL uptake and diffusion following FGF-2 treatment. Scale bar indicates 20 μm. **j**, Confocal representative images of Sca-1^{+} (green) arterial BVs in the metaphysis region. Note higher abundance of arterial BVs following FGF-2 treatment. Scale bar indicates 200 μm. **k**, For performance of homing assay, BM cells from c-Kit-EGFP labeled mice were lineage depleted, and transplanted to indicated recipient mice. Four hours post-transplantation bones from recipient mice were recovered, flushed and crushed, and the numbers of homed Lin^{-}/c-Kit-EGFP^{+}/Sca-1^{+}/CD34^{-} HSPCs were determined per femur by flow cytometry quantitative analysis. **l-q**, Mice were treated with FGF-2 (200 μg/kg) for 7 days. (Mean ± s.e.m., unless indicated otherwise n=12 mice from three independent experiments). P-values, two-tailed student's t-test (**P<0.01, ***P<0.005). **l**, HSPC homing per femur. (Mean ± s.e.m., n=8 mice from three independent experiments) **m**, Numbers of LSK HSPCs in the blood. **n**, Levels of chimerism indicating LTR-HSC contribution from blood transplant. (Mean ± s.e.m., n=20 mice from two independent experiments). **o**, Frequencies and representative density plots of BM αSMA^{+} pericytes as determined by flow cytometry analysis. **p-q**, Expression levels (MFI) and representative histograms of glucose uptake by HSPCs and MSPCs (respectively) were determined by flow cytometry analysis.

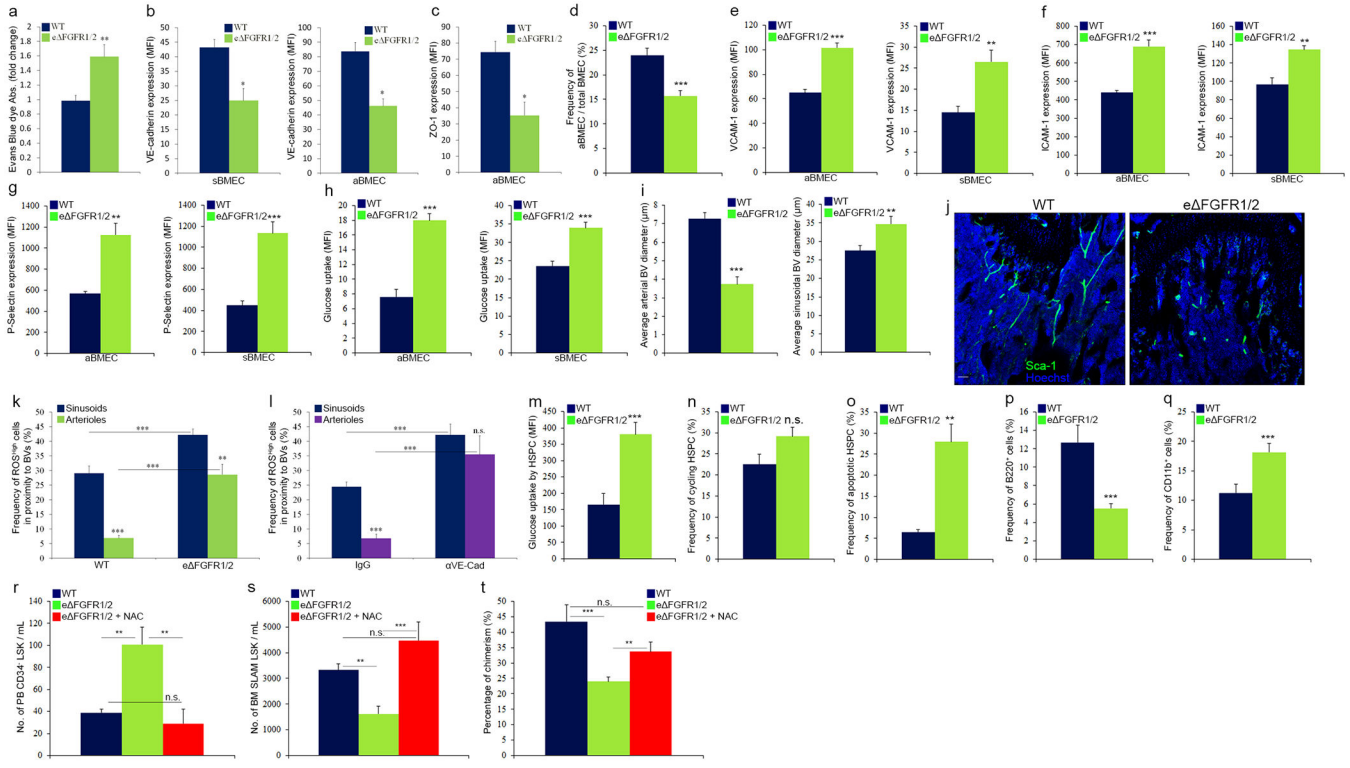

Extended Data figure 7:

a, EBD absorbance. (Mean ± s.e.m., n=6 mice from three independent experiments). P-values, two-tailed student's t-test (**P<0.01). **b-c**, Quantitative analysis of VE-cadherin and

ZO-1 MFIs on BMEC. (Mean ± s.e.m., n=6 mice from three independent experiments). P-values, two-tailed student's t-test (*P<0.05). **d-h**, Flow cytometry quantitative analysis of BMEC frequencies, surface and intracellular molecules expression (MFI), in WT or eΔFGFR1/2 mice. (Mean ± s.e.m., n=9 mice from three independent experiments). P-values, two-tailed student's t-test (**P<0.01, ***P<0.005). **i**, Diameters of distinct types of BM BVs in the metaphysis region as determined by ImageJ software analysis of high-resolution confocal images. **j**, Confocal representative images of Sca-1^{+} (green) arterial BVs in the metaphysis region. Note lower abundance of arterial BVs in eΔFGFR1/2 mice. Scale bar indicates 200 μm. **k-l**, (Mean ± s.e.m., n=16 BM sections were analyzed from n=4 mice). P-values, two-way ANOVA with Bonferroni's multiple comparison post-hoc test (**P<0.01, ***P<0.005). **k**, Frequency of ROS^{high} cells scored among total BM cells found in proximity (<20 μm) to different BM BVs, in WT or eΔFGFR1/2 mice. **l**, Frequency of ROS^{high} cells scored among total BM cells found in proximity (<20 μm) to different BM BVs, in C57BL/6 mice treated with neutralizing Rat anti VE-cadherin antibodies or Rat IgG control antibodies (50 μg/mouse/day) for 2 days. **m-o**, Flow cytometry quantitative analysis of (a) HSPC glucose uptake (MFI), frequency of (b) cycling HSPC and (c) apoptotic HSPC. (Mean ± s.e.m., n=9 mice from three independent experiments). P-values, two-tailed student's t-test (**P<0.01, ***P<0.005). **p-q**, Frequencies of donor derived lymphoid B220^{+} or myeloid CD11b^{+} cells in the PB of recipient mice, as were determined 24 weeks post transplantation by flow cytometry. (Mean ± s.e.m., n=18 donor mice from two independent experiments, for 3 recipient mice per donor). P-values, two-tailed student's t-test (***P<0.005). **r-t**, WT or eΔFGFR1/2 mice were treated with NAC (130 mg/kg) or PBS for 7 days. (Mean ± s.e.m., n=9 mice from three independent experiments). P-values, two-tailed student's t-test (**P<0.01, ***P<0.005). **r**, Number of circulating PB HSPC as determined by quantitative flow cytometry analysis. **s**, Number of BM SLAM LSK HSPC as determined by quantitative flow cytometry analysis. **t**, Levels of chimerism, indicating LTR-HSC contribution, were determined 24 weeks post transplantation by flow cytometry ratio analysis (CD45.2/(CD45.2+CD45.1)). (Mean ± s.e.m., n=24 donor mice from two independent experiments, for 3 recipient mice per donor).

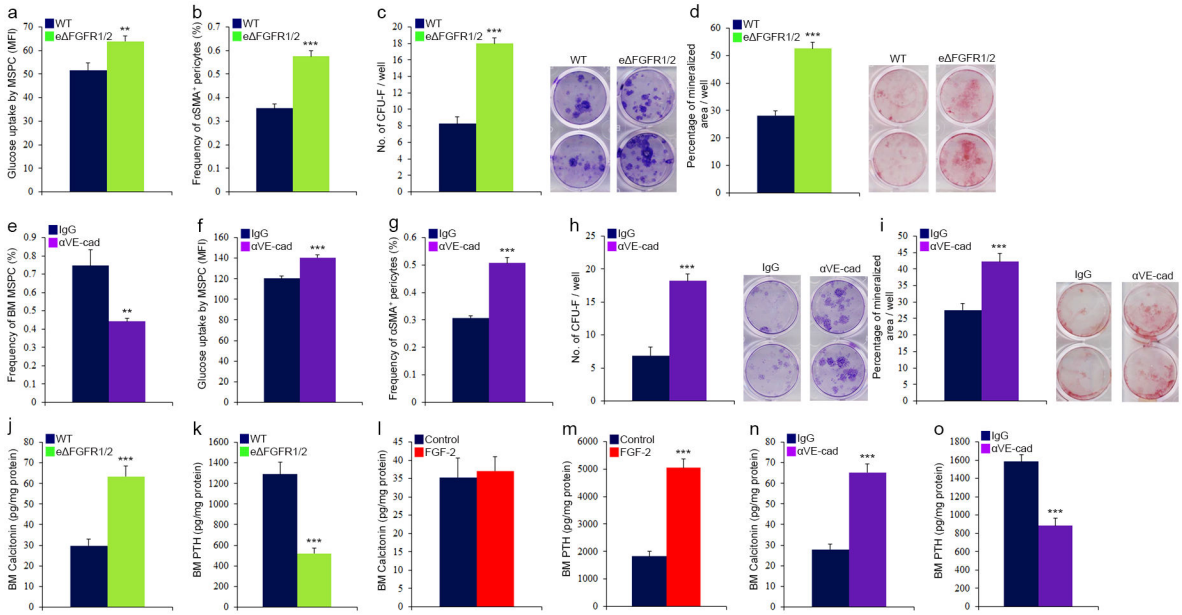

Extended Data figure 8:

a-d, (Mean ± s.e.m., n=9 mice from three independent experiments). P-values, two-tailed student's t-test (**P<0.01, ***P<0.005). **a**, Glucose uptake by BM MSPC as determined by quantitative flow cytometry (MFI) analysis. **b**, Frequencies of BM αSMA$^+$ pericytes as determined by flow cytometry analysis. **c**, Average number of scored (ImageJ) CFU-F per well and representative images. **d**, Average determined (ImageJ) percentage of mineralized area per well and representative images. **e-i**, C57BL/6 mice were treated with neutralizing Rat anti VE-cadherin antibodies or Rat IgG control antibodies (50 μg/mouse/day) for 5 days. (Mean ± s.e.m., n=9 mice from three independent experiments). P-values, two-tailed student's t-test and one-way ANOVA with Bonferroni's multiple comparison post-hoc test (**P<0.01, ***P<0.005). **e**, Frequency of BM MSPC as determined by flow cytometry quantitative analysis. **f**, Glucose uptake by BM MSPC as determined by quantitative flow cytometry (MFI) analysis. **g**, Frequencies of BM αSMA$^+$ pericytes as determined by flow cytometry analysis. **h**, Average number of scored (ImageJ) CFU-F per well and representative images. **i**, Average determined (ImageJ) percentage of mineralized area per well and representative images. **j-o**, BM supernatants from WT or eΔFGFR1/2, PBS or FGF-2 (200 μg/kg) treated for 7 days, and IgG or Rat anti VE-cadherin (50 μg/mouse/day) for 5 days, were isolated and BM concentrations of calcitonin and PTH hormones were determined using ELISA assay. (Mean ± s.e.m., n=9 mice per group from three independent experiments). P-values, two-tailed student's t-test (***P<0.005).

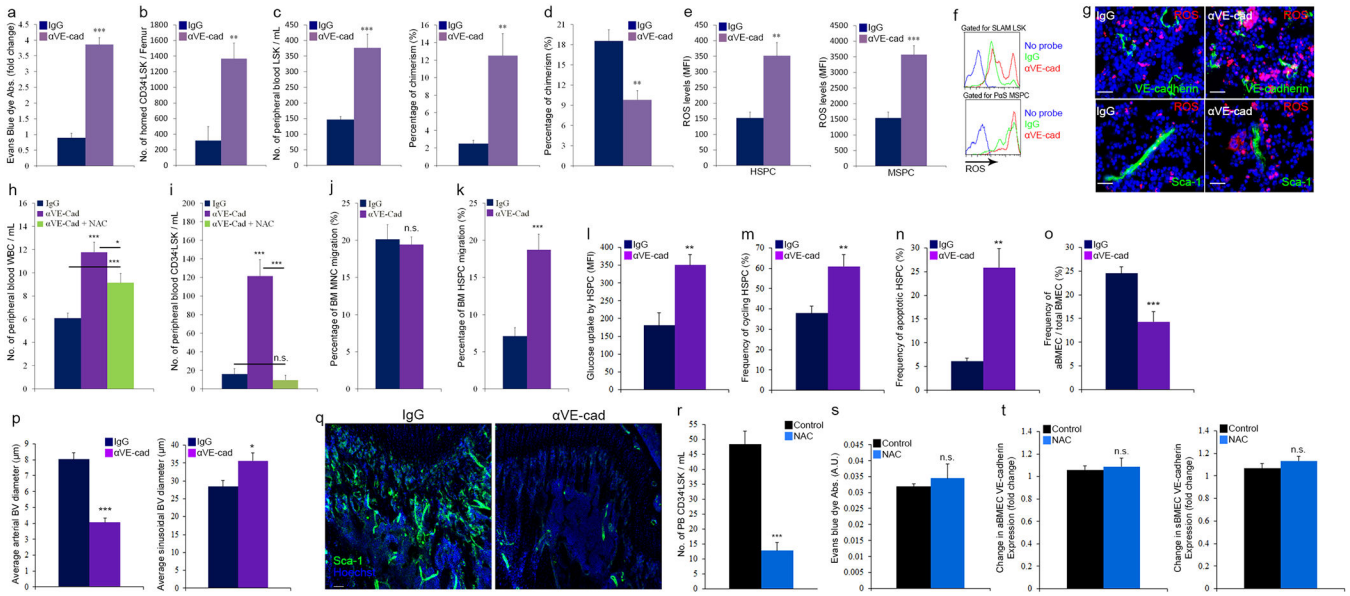

Extended Data figure 9:

a-j, C57BL/6 mice were treated with neutralizing Rat anti VE-cadherin antibodies or Rat IgG control antibodies (50 μg/mouse/day) for 5 days. (Mean ± s.e.m., unless otherwise indicated n=9 mice from three independent experiments). P-values, two-tailed student's t-test (*P<0.05, **P<0.01, ***P<0.005). **a**, EBD absorbance. **b**, HSPCs homing per femur. **c**, Quantitative analysis of blood LSK HSPC and chimerism levels indicating LTR-HSC contribution. (Mean ± s.e.m., n=10 mice from two independent experiments). **d**, Chimerism levels indicating LTR-HSC contribution. (Mean ± s.e.m., n=18 donor mice from two independent experiments, for 3 recipient mice per donor). **e-f**, Quantitative analysis and representative histogram plots of HSPCs and PαS MSPCs ROS MFI. **g**, Representative images of ROS^{High} (red) cells in proximity to BVs. Scale bar indicates 20 μm. **h-k**, C57BL/6 mice were treated with neutralizing Rat anti VE-cadherin antibodies or Rat IgG control antibodies (50 μg/mouse/day) for 2 days. Where indicated mice were also treated with NAC (130 mg/kg) or PBS for 2 days. (Mean ± s.e.m., n=9 mice from three independent experiments). P-values, two-tailed student's t-test and one-way ANOVA with Bonferroni's multiple comparison post-hoc test (*P<0.05, ***P<0.005). **h**, White blood cell (WBC) numbers in the blood circulation were determined using hematocytometer and Turk lysis of erythrocytes. **i**, Flow cytometry quantitative analysis of $CD34^{-}$ LSK HSPC in the blood circulation. **j-k**, BM MNC or BM lineage depleted cells from treated mice were seeded on a 5 μm pore transwell and allowed to migrate for 2 hours towards CXCL12 (125 ng/mL). Following migration the frequency of migrated BM MNC or $CD34^{-}$/LSK HSPC was determined by flow cytometry quantitative analysis. Note preferential HSPC enhanced migration post VE-cadherin neutralization. **l-p**, C57BL/6 mice were treated with neutralizing Rat anti VE-cadherin antibodies or Rat IgG control antibodies (50 μg/mouse/day) for 5 days. (Mean ± s.e.m., n=9 mice from three independent experiments). P-values, two-tailed student's t-test (**P<0.01, ***P<0.005). **l**, Glucose uptake levels (MFI) by HSPC as determined by flow cytometry quantitative analysis. **m-n**, Frequencies of $Ki67^{+}$ cycling and $AnnexinV^{+}$ SLAM LSK HSPC as determined by flow cytometry quantitative analysis.

o, Frequency of Sca-1$^+$ aBMEC out of total as determined by flow cytometry quantitative analysis. **p**, Diameters of distinct types of BM BVs in the metaphysis region as determined by ImageJ software analysis of high-resolution confocal images. **q**, Confocal representative images of Sca-1$^+$ (green) arterial BVs in the metaphysis region. Note lower abundance of arterial BVs following 5 days anti VE-cadherin treatment. Scale bar indicates 200 μm. **r-t**, C57BL/6 mice were treated with NAC (130 mg/kg) or PBS for 7 days. (Mean ± s.e.m., n=8 mice from two independent experiments). P-values, two-tailed student's t-test (***P<0.005). **r**, Flow cytometry quantitative analysis of CD34$^-$ LSK HSPC in the blood circulation. **s**, EBD absorbance following extraction from the femur was measured using spectrophotometric analysis at 620 nm and 740 nm. **t**, VE-cadherin expression levels (MFI) on distinct types of BMEC as determined by flow cytometry quantitative analysis (arterial and sinusoidal respectively).

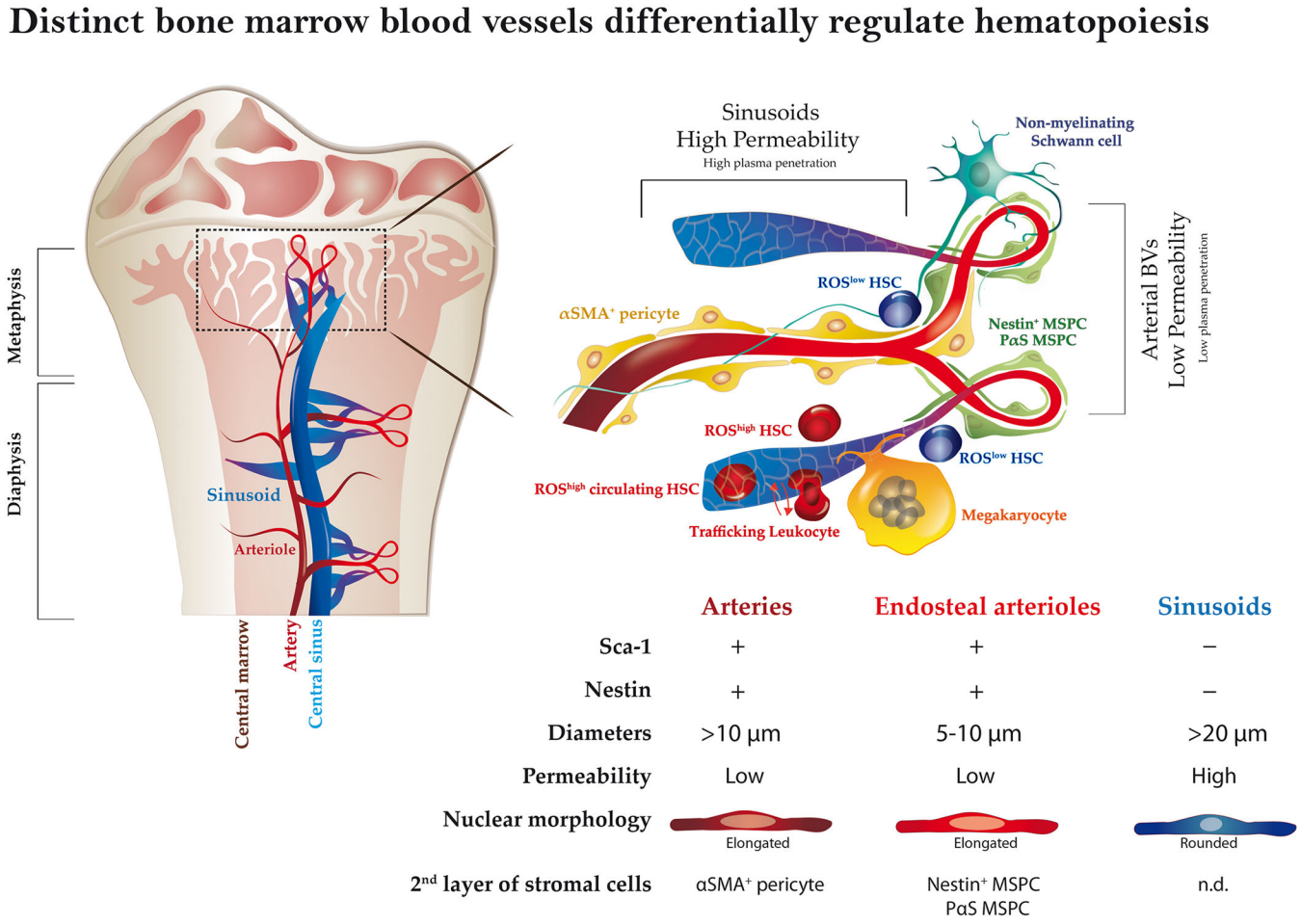

Extended Data figure 10: Illustration proposed BM BVs model and regulation of hematopoiesis. BM vasculature is composed of two main types of blood vessels which are arterial BVs, and sinusoids. Blood enters the BM via the arteries, branching to smaller arterioles, which in proximity to endosteal areas, further branch into small-diameter endosteal arterioles. These endosteal arterioles reconnect to downstream sinusoids which drain the blood into the central sinus and out of the BM. Arterial BMEC have elongated nuclear morphology,

express Sca-1 and nestin markers, and display high barrier integrity properties. In addition arterial BVs display the highest blood flow speed and shear rate. Arterial BMEC maintain a microenvironment that promotes low ROS state of HSCs in its surrounding. The second layer of cells associated with arteries is composed of αSMA^{+} pericytes while endosteal arterioles are associated with HSC-supportive MSPCs. The association of MSPCs and ROS^{low} HSCs with endosteal capillaries suggests the existence of an osteo-vascular niche where the residing HSCs are influenced by both endosteal and vascular elements simultaneously. Also, innervating Schwann cell nerve fibers, shown to maintain HSC dormancy, were found to be associated with arteries and endosteal arterioles. More permeable fenestrated sinusoids induce higher ROS state in their surroundings, and have slower internal blood flow, all which makes them the ultimate candidate to serve as the site for BM cellular trafficking. Megakaryocytes found in sinusoidal sites support and maintain HSPC in a ROS low state. Live real time imaging indicates that all leukocyte trafficking occurs exclusively via sinusoids. Furthermore, experimental systems manipulating endothelial barrier integrity provide evidence that more fenestrated endothelial state promotes trafficking at the expanse of stem cell maintenance. Yet, conditions enhancing endothelial integrity, reducing cellular trafficking promote BM stem cell expansion and maintenance. PB plasma, which can penetrate into the BM more easily via fenestrated BVs, enhances HSPC migratory capacity but hampers their long term repopulation capacity and survival. Thus, the state of the endothelial blood-bone marrow-barrier in distinct BVs and under steady state or “stress” conditions may have a strong regulatory impact on tissue residing stem cells.

Supplementary Material

Refer to Web version on PubMed Central for supplementary material.

ACKNOWLEGMENTS:

We thank Prof. Gerard Karsenty (Columbia University) and Prof. Marshall A. Lichtman (University of Rochester) for fruitful discussions and for critically reviewing the manuscript. We thank Dr. Simón Méndez-Ferrer and Dr. Maria Argueta Hernandez for fruitful discussions and assistance in studies involving MSPCs and nervous system elements. We thank Dr. Ziv Porat for technical assistance with ImageStream analysis and Dr. Ron Rotkopf for assistance with statistical data analysis. This study was partially supported by the Ministry of Science, Technology & Space, Israel and the DKFZ, Germany, grants from the Israel Science Foundation (851/13), the Ernest and Bonnie Beutler Research Program of Excellence in Genomic Medicine and EU FP7-HEALTH-2010 (CELL-PID #261387) (T.L.). Confocal studies were supported by the European Research Council Advanced Grant 339409, ‘AngioBone’ (R.H.A.). Intravital multiphoton studies were supported by NIH grants EB017274 and HL100402 (C.P.L. & D.T.S.).

References

1. Rafii S, Butler JM & Ding BS Angiocrine functions of organ-specific endothelial cells. Nature 529, 316–325 (2016). [PubMed: 26791722]
2. Lapidot T, Dar A & Kollet O How do stem cells find their way home? Blood 106, 1901–1910 (2005). [PubMed: 15890683]
3. Morrison SJ & Scadden DT The bone marrow niche for haematopoietic stem cells. Nature 505, 327–334 (2014). [PubMed: 24429631]
4. Kusumbe AP, Ramasamy SK & Adams RH Coupling of angiogenesis and osteogenesis by a specific vessel subtype in bone. Nature 507, 323–328 (2014). [PubMed: 24646994]

5. Kiel MJ, Yilmaz OH, Iwashita T, Terhorst C & Morrison SJ SLAM family receptors distinguish hematopoietic stem and progenitor cells and reveal endothelial niches for stem cells. Cell 121, 1109–1121 (2005). [PubMed: 15989959]
6. Sipkins DA, et al. In vivo imaging of specialized bone marrow endothelial microdomains for tumour engraftment. Nature 435, 969–973 (2005). [PubMed: 15959517]
7. Colmone A, et al. Leukemic cells create bone marrow niches that disrupt the behavior of normal hematopoietic progenitor cells. Science 322, 1861–1865 (2008). [PubMed: 19095944]
8. Lo Celso C, et al. Live-animal tracking of individual haematopoietic stem/progenitor cells in their niche. Nature 457, 92–96 (2009). [PubMed: 19052546]
9. Mendez-Ferrer S, et al. Mesenchymal and haematopoietic stem cells form a unique bone marrow niche. Nature 466, 829–834 (2010). [PubMed: 20703299]
10. Ding L, Saunders TL, Enikolopov G & Morrison SJ Endothelial and perivascular cells maintain haematopoietic stem cells. Nature 481, 457–462 (2012). [PubMed: 22281595]
11. Kunisaki Y, et al. Arteriolar niches maintain haematopoietic stem cell quiescence. Nature 502, 637–643 (2013). [PubMed: 24107994]
12. Hooper AT, et al. Engraftment and reconstitution of hematopoiesis is dependent on VEGFR2-mediated regeneration of sinusoidal endothelial cells. Cell Stem Cell 4, 263–274 (2009). [PubMed: 19265665]
13. Isern J, et al. The neural crest is a source of mesenchymal stem cells with specialized hematopoietic stem cell niche function. Elife 3, e03696 (2014). [PubMed: 25255216]
14. Ito K, et al. Reactive oxygen species act through p38 MAPK to limit the lifespan of hematopoietic stem cells. Nat Med 12, 446–451 (2006). [PubMed: 16565722]
15. Miyamoto K, et al. Foxo3a is essential for maintenance of the hematopoietic stem cell pool. Cell Stem Cell 1, 101–112 (2007). [PubMed: 18371339]
16. Tesio M, et al. Enhanced c-Met activity promotes G-CSF-induced mobilization of hematopoietic progenitor cells via ROS signaling. Blood 117, 419–428 (2011). [PubMed: 20585044]
17. Golan K, et al. S1P promotes murine progenitor cell egress and mobilization via S1P1-mediated ROS signaling and SDF-1 release. Blood 119, 2478–2488 (2012). [PubMed: 22279055]
18. Zhao M, et al. Megakaryocytes maintain homeostatic quiescence and promote post-injury regeneration of hematopoietic stem cells. Nat Med 20, 1321–1326 (2014). [PubMed: 25326798]
19. Bruns I, et al. Megakaryocytes regulate hematopoietic stem cell quiescence through CXCL4 secretion. Nat Med 20, 1315–1320 (2014). [PubMed: 25326802]
20. Nakamura-Ishizu A, Takubo K, Fujioka M & Suda T Megakaryocytes are essential for HSC quiescence through the production of thrombopoietin. Biochem Biophys Res Commun 454, 353–357 (2014). [PubMed: 25451253]
21. Nombela-Arrieta C, et al. Quantitative imaging of haematopoietic stem and progenitor cell localization and hypoxic status in the bone marrow microenvironment. Nat Cell Biol 15, 533–543 (2013). [PubMed: 23624405]
22. Ono N, et al. Vasculature-associated cells expressing nestin in developing bones encompass early cells in the osteoblast and endothelial lineage. Dev Cell 29, 330–339 (2014). [PubMed: 24823376]
23. Ludin A, et al. Monocytes-macrophages that express alpha-smooth muscle actin preserve primitive hematopoietic cells in the bone marrow. Nat Immunol 13, 1072–1082 (2012). [PubMed: 22983360]
24. Yamazaki S, et al. Nonmyelinating Schwann cells maintain hematopoietic stem cell hibernation in the bone marrow niche. Cell 147, 1146–1158 (2011). [PubMed: 22118468]
25. Papayannopoulou T, Priestley GV, Nakamoto B, Zafiropoulos V & Scott LM Molecular pathways in bone marrow homing: dominant role of alpha(4)beta(1) over beta(2)-integrins and selectins. Blood 98, 2403–2411 (2001). [PubMed: 11588037]
26. Winkler IG, et al. Vascular niche E-selectin regulates hematopoietic stem cell dormancy, self renewal and chemoresistance. Nat Med 18, 1651–1657 (2012). [PubMed: 23086476]
27. De Bock K, et al. Role of PFKFB3-driven glycolysis in vessel sprouting. Cell 154, 651–663 (2013). [PubMed: 23911327]

28. Vandekeere S, Dewerchin M & Carmeliet P Angiogenesis Revisited: An Overlooked Role of Endothelial Cell Metabolism in Vessel Sprouting. Microcirculation 22, 509–517 (2015). [PubMed: 26250801]
29. Spencer JA, et al. Direct measurement of local oxygen concentration in the bone marrow of live animals. Nature 508, 269–273 (2014). [PubMed: 24590072]
30. Broxmeyer HE, et al. Rapid mobilization of murine and human hematopoietic stem and progenitor cells with AMD3100, a CXCR4 antagonist. J Exp Med 201, 1307–1318 (2005). [PubMed: 15837815]
31. Heissig B, et al. Recruitment of stem and progenitor cells from the bone marrow niche requires MMP-9 mediated release of kit-ligand. Cell 109, 625–637 (2002). [PubMed: 12062105]
32. Dar A, et al. Rapid mobilization of hematopoietic progenitors by AMD3100 and catecholamines is mediated by CXCR4-dependent SDF-1 release from bone marrow stromal cells. Leukemia 25, 1286–1296 (2011). [PubMed: 21494253]
33. Kobayashi K, et al. Stromal cell-derived factor-1alpha/C-X-C chemokine receptor type 4 axis promotes endothelial cell barrier integrity via phosphoinositide 3-kinase and Rac1 activation. Arterioscler Thromb Vasc Biol 34, 1716–1722 (2014). [PubMed: 24925969]
34. Itkin T, et al. FGF-2 expands murine hematopoietic stem and progenitor cells via proliferation of stromal cells, c-Kit activation, and CXCL12 down-regulation. Blood 120, 1843–1855 (2012). [PubMed: 22645180]
35. Zhao M, et al. FGF signaling facilitates postinjury recovery of mouse hematopoietic system. Blood 120, 1831–1842 (2012). [PubMed: 22802336]
36. Murakami M, et al. The FGF system has a key role in regulating vascular integrity. J Clin Invest 118, 3355–3366 (2008). [PubMed: 18776942]
37. De Smet F, et al. Fibroblast growth factor signaling affects vascular outgrowth and is required for the maintenance of blood vessel integrity. Chem Biol 21, 1310–1317 (2014). [PubMed: 25200605]
38. Houlihan DD, et al. Isolation of mouse mesenchymal stem cells on the basis of expression of Sca-1 and PDGFR-alpha. Nat Protoc 7, 2103–2111 (2012). [PubMed: 23154782]
39. Wei J, et al. Glucose Uptake and Runx2 Synergize to Orchestrate Osteoblast Differentiation and Bone Formation. Cell 161, 1576–1591 (2015). [PubMed: 26091038]
40. Fujita K, et al. Vitamin E decreases bone mass by stimulating osteoclast fusion. Nat Med 18, 589–594 (2012). [PubMed: 22388090]
41. Cohen SG, et al. PAR1 signaling regulates the retention and recruitment of EPCR-expressing bone marrow hematopoietic stem cells. Nat Med 21, 1307–1317 (2015). [PubMed: 26457757]
42. Zhang J, et al. Identification of the haematopoietic stem cell niche and control of the niche size. Nature 425, 836–841 (2003). [PubMed: 14574412]
43. Arai F, et al. Tie2/angiopoietin-1 signaling regulates hematopoietic stem cell quiescence in the bone marrow niche. Cell 118, 149–161 (2004). [PubMed: 15260986]
44. Sugimura R, et al. Noncanonical Wnt signaling maintains hematopoietic stem cells in the niche. Cell 150, 351–365 (2012). [PubMed: 22817897]
45. Xie Y, et al. Detection of functional haematopoietic stem cell niche using real-time imaging. Nature 457, 97–101 (2009). [PubMed: 19052548]
46. Bear MD, et al. Alpha-Catulin Co-Localizes With Vimentin Intermediate Filaments and Functions in Pulmonary Vascular Endothelial Cell Migration via ROCK. J Cell Physiol (2015).
47. Acar M, et al. Deep imaging of bone marrow shows non-dividing stem cells are mainly perisinusoidal. Nature 526, 126–130 (2015). [PubMed: 26416744]
48. Mantel CR, et al. Enhancing Hematopoietic Stem Cell Transplantation Efficacy by Mitigating Oxygen Shock. Cell 161, 1553–1565 (2015). [PubMed: 26073944]
49. Shen H, et al. An acute negative bystander effect of gamma-irradiated recipients on transplanted hematopoietic stem cells. Blood 119, 3629–3637 (2012). [PubMed: 22374698]
50. Hu L, et al. Antioxidant N-acetyl-L-cysteine increases engraftment of human hematopoietic stem cells in immune-deficient mice. Blood 124, e45–48 (2014). [PubMed: 25287706]

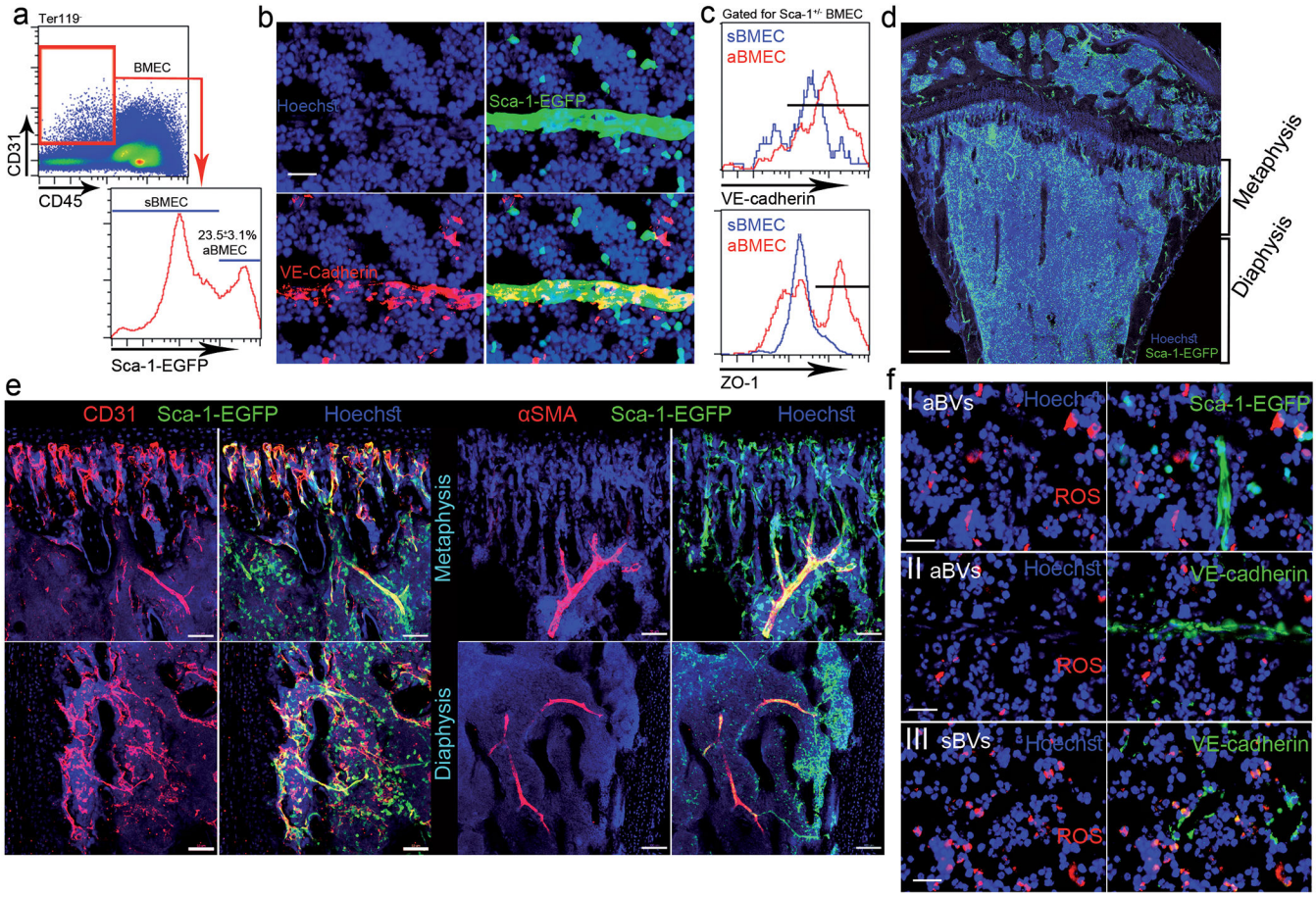

Figure 1: Sca-1 and nestin distinguish less permeable arterial BM BVs, which sustain ROS^{low} HSC.

a, Representative flow cytometry density and histogram plots for BMECs. (Mean ± s.e.m., n=6 mice from three independent experiments). **b**, Representative fluorescence images of a small diameter blood vessel from the metaphysial area expressing Sca-1-EGFP (green), junctional VE-cadherin (red) and elongated nuclei (Hoechst, blue). Scale bar indicates 20 μm. **c**, VE-cadherin and ZO-1 flow cytometry representative histogram plots for mean fluorescent expression (MFI) by BMECs. (n=9 mice from three independent experiments). **d**, Representative confocal tile scan of Sca-1-EGFP (Green) femur. Scale bar indicates 300 μm. **e**, Representative confocal images of endosteal regions in the metaphysis and diaphysis showing Sca-1$^+$ (green)/CD31$^+$ (red) arterial BVs and αSMA$^+$ (red) pericytes. Scale bars in panels indicate 50 μm except for lower right panel where scale bar indicates 100 μm. **f**, Representative fluorescence images of ROS^{high} (red) expressing cells in the proximate microenvironment of Sca-1$^+$ (green) or VE-cadherin$^+$ (green) arterioles (I, II respectively) and VE-cadherin$^+$ (green) sinusoids (III). Scale bar indicates 20 μm.

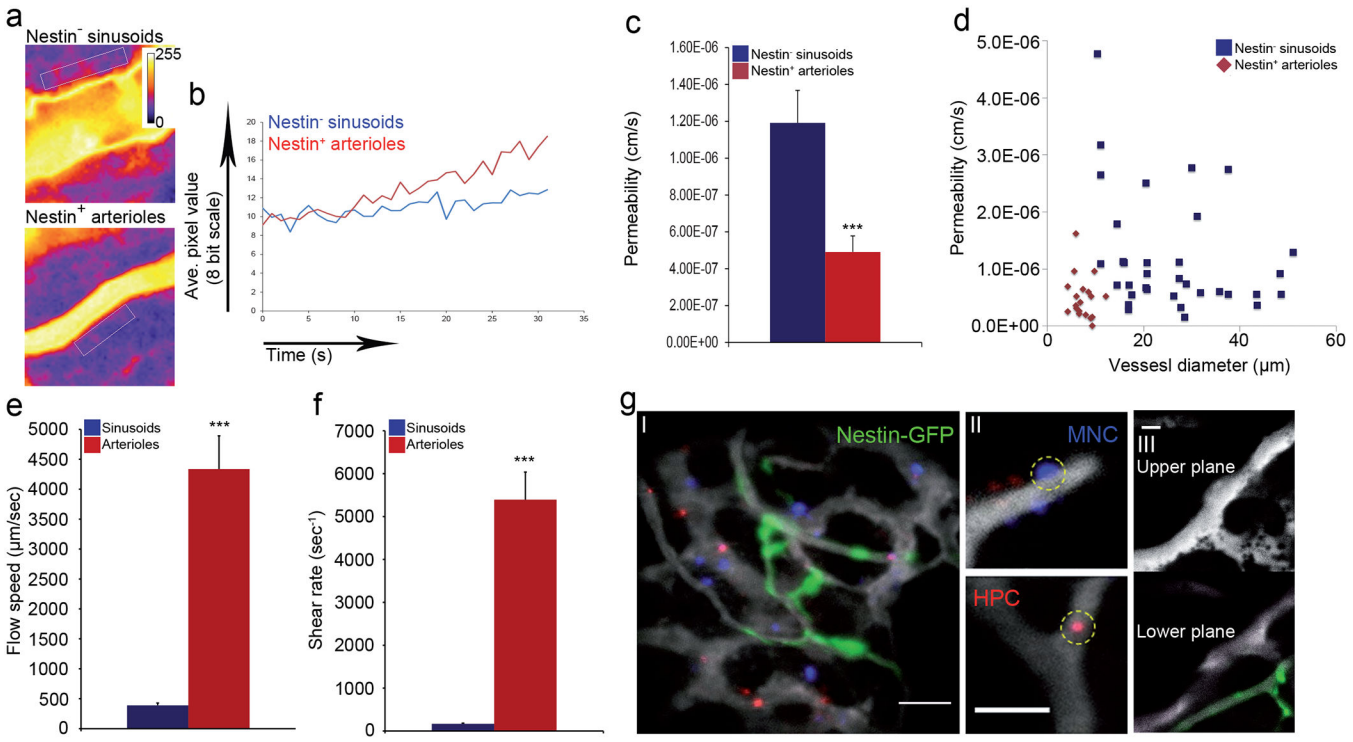

Figure 2: Leaky sinusoids are the exclusive site for cellular trafficking.

a-g, (Mean ± s.e.m., n=53 BVs were analyzed for permeability measurements and n=62 BVs were analyzed for blood flow/shear rates, from three independent experiments each). P-values, two-tailed student's t-test (***P<0.005). **a**, Standard deviation heat map of Rhodamine-Dextran leakage. Color scale shows pixel intensity over 30 seconds of data acquisition. Regions of interest are bordered with white line. **b**, Time traces of fluorescence signal. **c**, Average vascular permeability. **d**, A plot of permeability measurements as a function of vessel diameter. **e-f**, Average blood flow speed and shear rate. **g**, Representative maximum intensity images demonstrating (I) homing of adoptively transferred lineage depleted HPC (hematopoietic progenitor cell, red) and BM MNC (blue) within the BM of a nestin-GFP (green) mouse, (II) transmigrating BM MNC (circled, blue) and adherent Lin^{-} HPC (circled, red)(Scale bars indicate 50 μm), (III) upper and lower planes of the Z-stack taken from supplementary video 9 representing the relative proximity of a $nestin^{+}$ BV to a sinusoidal trafficking site (Scale bar indicates 25 μm, n=309 trafficking events were monitored and analyzed).

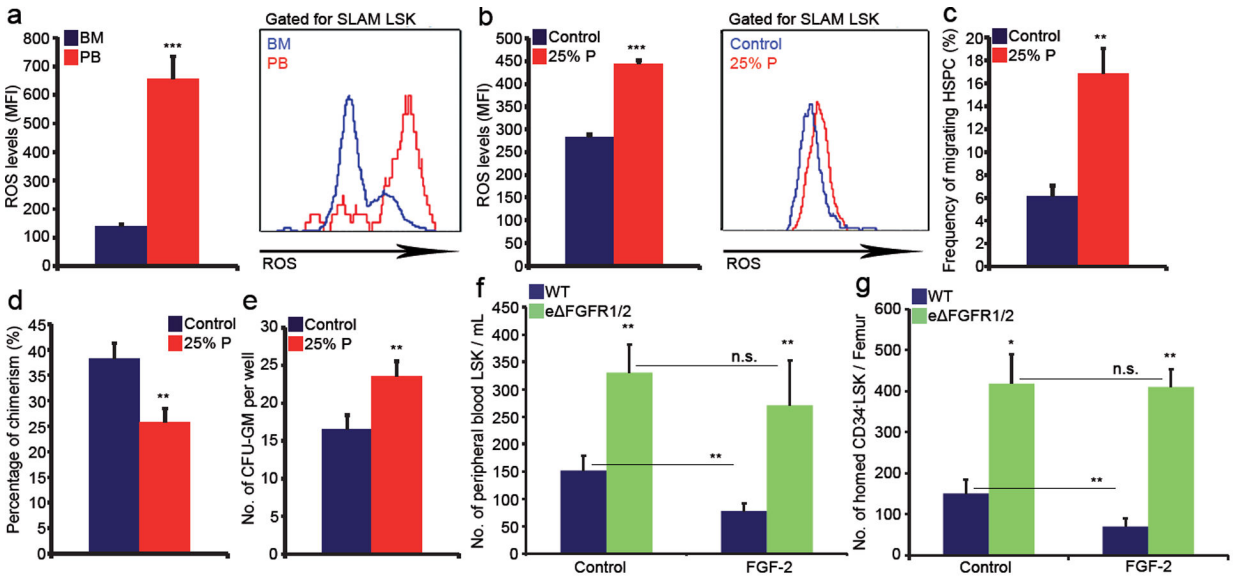

Figure 3: Plasma penetration through leaky endothelium dictates HSPC trafficking and development.

a, HSPCs ROS MFI quantitative analysis and representative histogram plot. (Mean ± s.e.m., n=6 mice from three independent experiments). P-values, two-tailed student's t-test (***P<0.005). **b-e**, BM cells were incubated for 2h with (25% P) or without (control) PB plasma. (Mean ± s.e.m., n=9 repeats in triplicates from three independent experiments). P-values, two-tailed student's t-test (**P<0.01, ***P<0.005). **b**, HSPCs ROS MFI quantitative analysis and representative histogram plot. **c**, HSPC migration frequency. **d**, Chimerism levels indicating LTR-HSC contribution. (Mean ± s.e.m., n=27 donor from three independent experiments, with at least 3 recipient mice per donor). **e**, Average number of CFU-GM. **f**, Numbers of LSK HSPCs in the blood. (Mean ± s.e.m., n=9 mice from three independent experiments). P-values, two-way ANOVA with Bonferroni's multiple comparison post-hoc test (**P<0.01). **g**, HSPC homing per femur. (Mean ± s.e.m., n=5 mice from 2 independent experiments). P-values, two-way ANOVA with Bonferroni's multiple comparison post-hoc test (*P<0.05, **P<0.01).

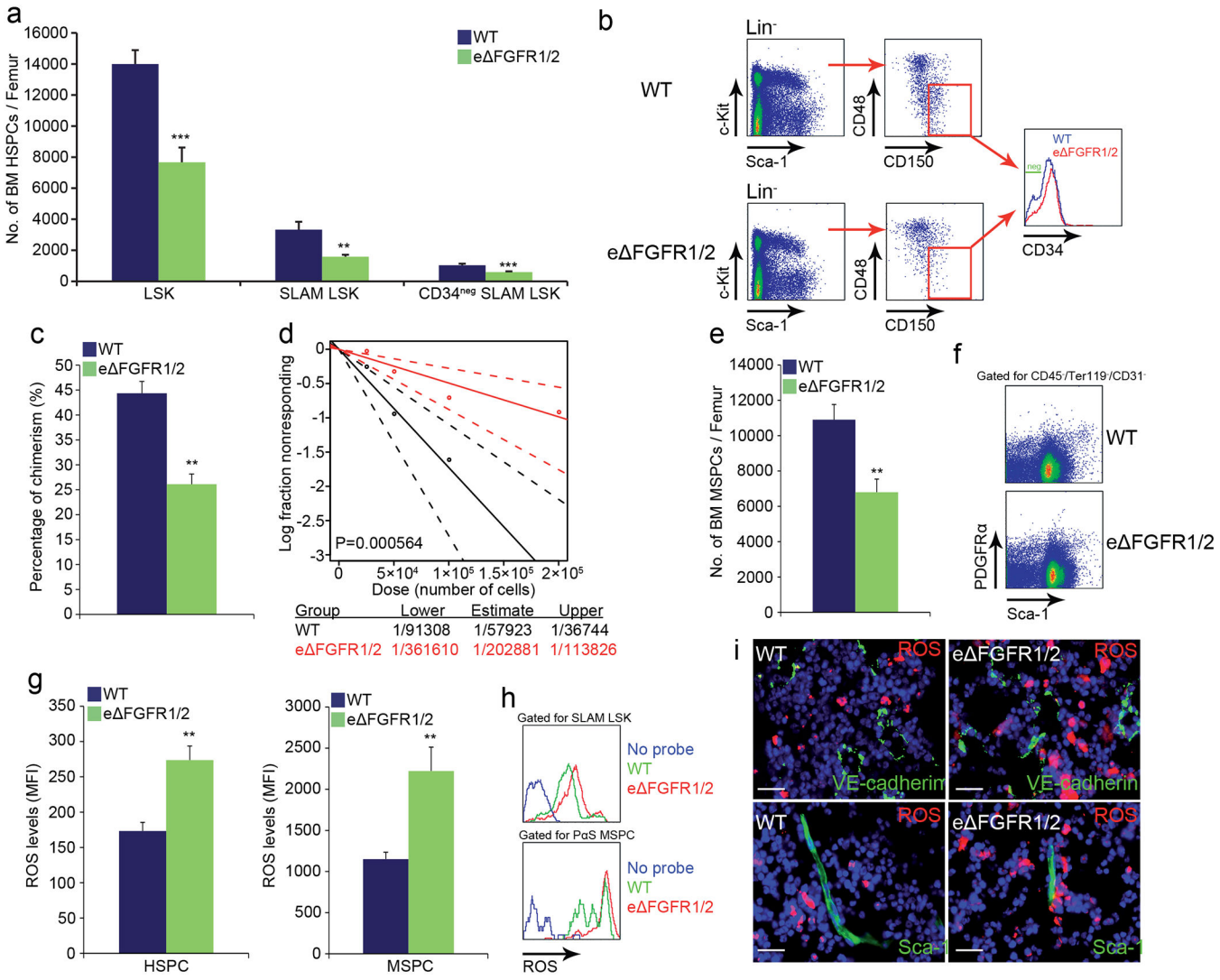

Figure 4: Reducing endothelial barrier integrity hampers stem cell maintenance.

a-h, (Mean ± s.e.m., n=9 mice from three independent experiments). P-values, two-tailed student's t-test (**P<0.01, ***P<0.005). **a-b**, Quantitative analysis and representative plots of HSPC populations. **c**, Chimerism levels indicating LTR-HSC contribution. (Mean ± s.e.m., n=18 donor mice from two independent experiments, with 3 recipient mice per donor). **d**, Repopulating units frequency in the BM indicating HSC. (n=60 donor mice from two independent experiments, for 3 recipient mice per dilution per donor). **e-f**, Quantitative analysis and representative density plots of MSPCs. **g-h**, Quantitative analysis and representative histogram plots of HSPCs and PαS MSPCs ROS MFIs. **i**, Representative images of ROS^{High} (red) cells in proximity to BVs. Scale bar indicates 20 μm.